

A TRIDENT SCHOLAR PROJECT REPORT

NO. 470

**A Microlensing Analysis of the Central Engine in the
Lensed Quasar WFI J2033-4723**

by

Midshipman 1/C Gregory E. Hyer, USN



UNITED STATES NAVAL ACADEMY
ANNAPOLIS, MARYLAND

This document has been approved for public
release and sale; its distribution is unlimited.

REPORT DOCUMENTATION PAGE				Form Approved OMB No. 0704-0188	
Public reporting burden for this collection of information is estimated to average 1 hour per response, including the time for reviewing instructions, searching existing data sources, gathering and maintaining the data needed, and completing and reviewing this collection of information. Send comments regarding this burden estimate or any other aspect of this collection of information, including suggestions for reducing this burden to Department of Defense, Washington Headquarters Services, Directorate for Information Operations and Reports (0704-0188), 1215 Jefferson Davis Highway, Suite 1204, Arlington, VA 22202-4302. Respondents should be aware that notwithstanding any other provision of law, no person shall be subject to any penalty for failing to comply with a collection of information if it does not display a currently valid OMB control number. PLEASE DO NOT RETURN YOUR FORM TO THE ABOVE ADDRESS.					
1. REPORT DATE (DD-MM-YYYY) 05-21-18		2. REPORT TYPE		3. DATES COVERED (From - To)	
4. TITLE AND SUBTITLE A Microlensing Analysis of the Central Engine in the Lensed Quasar WFI J2033-4723				5a. CONTRACT NUMBER	
				5b. GRANT NUMBER	
				5c. PROGRAM ELEMENT NUMBER	
6. AUTHOR(S) Hyer, Gregory E.				5d. PROJECT NUMBER	
				5e. TASK NUMBER	
				5f. WORK UNIT NUMBER	
7. PERFORMING ORGANIZATION NAME(S) AND ADDRESS(ES)				8. PERFORMING ORGANIZATION REPORT NUMBER	
9. SPONSORING / MONITORING AGENCY NAME(S) AND ADDRESS(ES) U.S. Naval Academy Annapolis, MD 21402				10. SPONSOR/MONITOR'S ACRONYM(S)	
				11. SPONSOR/MONITOR'S REPORT NUMBER(S) Trident Scholar Report no. 470 (2018)	
12. DISTRIBUTION / AVAILABILITY STATEMENT This document has been approved for public release; its distribution is UNLIMITED.					
13. SUPPLEMENTARY NOTES					
14. ABSTRACT We measured the size of the accretion disk in the gravitationally lensed quasar WFI J2033-4723 by the analysis of 13 seasons of optical imagery. Using point spread function (PSF) modeling software, we measured the brightness of each of this system's four images in 7 seasons of optical monitoring data taken at the 1.3m SMARTS telescope at Cerro Tololo, Chile and in 6 seasons of optical monitoring data from the 1.5m EULER telescope in La Silla, Chile. We combined these new data with published measurements from Vuissoz et al. (2008) to create a 13-season set of optical light curves. Employing the Bayesian Monte Carlo microlensing analysis technique of Kochanek (2004), we analyzed these light curves to yield the first-ever measurement of the size of this quasar's accretion disk $\log\{(r_s/\text{cm})[\cos(i)/0.5]^{1/2}\} = 15.86^{+0.25}_{-0.27}$ at the rest frame center of the R-band $\lambda_{\text{rest}} = 247$ nm. Despite the fact that we now know of ~ 106 lensed quasars, the size of the central engine has been measured in only 14 of these systems.					
15. SUBJECT TERMS cosmology, accretion, accretion disks, dark matter, gravitational lensing, quasars					
16. SECURITY CLASSIFICATION OF:			17. LIMITATION OF ABSTRACT	18. NUMBER OF PAGES 38	19a. NAME OF RESPONSIBLE PERSON
a. REPORT	b. ABSTRACT	c. THIS PAGE			19b. TELEPHONE NUMBER (include area code)

U.S.N.A. – Trident Scholar project report; no. 470 (2018)

A MICROLENSING ANALYSIS OF THE
CENTRAL ENGINE IN THE
LENSED QUASAR WFI J2033-4723

by

Midshipman 1/C Gregory E. Hyer
United States Naval Academy
Annapolis, Maryland

Certification of Advisers Approval

Associate Professor Christopher W. Morgan
Physics Department

Professor Jeffrey A. Larsen
Physics Department

Acceptance for the Trident Scholar Committee
Submitted to the Trident Scholar Committee April 2018

Professor Maria Schroeder

ABSTRACT

We measured the size of the accretion disk in the gravitationally lensed quasar WFI J2033-4723 by the analysis of 13 seasons of optical imagery. Using point spread function (PSF) modeling software, we measured the brightness of each of this system's four images in 7 seasons of optical monitoring data taken at the the 1.3m SMARTS telescope at Cerro Tololo, Chile and in 6 seasons of optical monitoring data from the 1.5m EULER telescope in La Silla, Chile. We combined these new data with published measurements from Vuissoz et al. (2008) to create a 13-season set of optical light curves. Employing the Bayesian Monte Carlo microlensing analysis technique of Kochanek (2004), we analyzed these light curves to yield the first-ever measurement of the size of this quasar's accretion disk $\log\{(r_s/\text{cm})[\cos(i)/0.5]^{1/2}\} = 15.86^{+0.25}_{-0.27}$ at the rest frame center of the R-band $\lambda_{rest} = 247$ nm. Despite the fact that we now know of ~ 106 lensed quasars, the size of the central engine has been measured in only 14 of these systems.

Subject headings: cosmology: observations — accretion, accretion disks — dark matter — gravitational lensing — quasars: general

ACKNOWLEDGEMENTS

This year long project was in fact a four year effort involving the support of many people. Rather than attempt the impossible task of ranking the help I received in order of importance, I will copy my wiser predecessors, and move through this section chronologically in the hope of not making any glaring omissions. Firstly, I have to thank my parents for teaching me the importance of continuously learning and for passing on some of their insatiable literary appetites to me. The text within this report is in no small part a product of many years of patient grammar corrections, articles, poems, and books carefully procured from their dozens of years of reading. Moreover, their constant love, support, and desire to understand what I'm doing despite studying in a field far outside their own experiences has and continues to mean more than these few words can adequately express.

Many teachers prior to coming to the Naval Academy have had an enormous impact on me. Although I cannot list them all here, I must at least acknowledge my high school physics teacher, Mrs. Estrella. Her incredible energy, patience, and love for the subject inspired me to study physics in college. She even continues to teach and inspire the next generation of students to this day despite fighting pancreatic cancer.

The Navy Varsity Squash team and Coach Dawson have supported me through incredibly tough times and the team over the past four years here has truly become a second family to me. I couldn't think of a better group of guys on the planet. You all have made the hundreds of 55s, 300s, four "Christmas Days", and early mornings sleeping on the locker room floor some of the fondest memories of my life.

I also have to thank Professor Larsen who had the largely overlooked and thankless task of getting me off the ground with this project while Professor Morgan was still in Kuwait. In addition, Professor Albert and Katz were always there to give sound advice and support throughout my tenure as an astrophysics major. Professor Witt was an invaluable resource in helping us use the USNA High Performance Computing Cluster. Among these people whom I cannot adequately thank enough is Professor Malek-Madani, who was a mentor to me from the first day of classes and continues to be to this day. Many of the people above have written slews of recommendation letters and given hours of their time to selflessly helping me in various ways that I cannot sufficiently thank them enough for.

Lastly yet most notably, I thank Professor Morgan. He has devoted countless hours despite a hectic schedule from Kuwait to school-pickups, in patiently helping me through whatever new crisis I would either create or encounter in the pursuit of trying to complete this project. He has taught me that real science is messy, "deals with uncertainty", and at its core is profoundly human. Despite innumerable mistakes, explanations, and re-explanations he couldn't have been more unwaveringly positive and patient in helping me navigate not only the science but also the "roller-coaster ride" of the past four years. The word "thanks" seriously lacks the deep sense of gratitude and pride I feel in having been your student for the past four years.

Contents

1	Introduction	4
2	Background	5
2.1	Description of Observational Properties	5
2.2	Model for the Source of the Continuum Emission: SMBH Accretion	6
2.3	Introduction to Gravitational Lensing	7
2.4	Introduction to WFI 2033-4723	9
3	Observations and Data Reduction	11
4	Microlensing Analysis	15
5	Results and Discussion	20
5.1	Results	20
5.2	Discussion	21
6	Conclusions	23
	References	25
A	Reduced Photometric Data	27
B	Glossary of Terms	37

1. Introduction

Quasars, or “active galactic nuclei” (AGN), are the most luminous sources in the universe, but the accretion disks surrounding supermassive black holes in quasars are too compact to be spatially resolved with existing telescopes. Thus, the standard picture of the structure of these accretion disks is based mostly upon theoretical models rather than concrete observational measurements. However, in the case of gravitationally lensed quasars, the relative motions of the quasar source, lensing galaxy, stars within the lensing galaxy, and the observer create uncorrelated variations in the source magnification as a function of time and wavelength. This phenomenon is known as “microlensing”. These uncorrelated variations in the source magnification are dependent upon the projected area of the source quasar.

Analysis of the variations in brightness due to microlensing using numerical simulations can yield measurements of the size of the quasar accretion disk (Chang & Refsdal, 1979; Kochanek, 2004). These measurements are vital observational tests of theoretical models of accretion disk structure. To date there are two existing techniques for microlensing analysis. The first involves a multi-wavelength study of a lensed quasar over a small time period in which flux ratios of the images deviate from predictions of macroscopic lens models or show significant wavelength dependence (e.g. Mediavilla, 2011). The second method employs an analysis of the time variability of the quasar’s flux ratio over a much longer period of time. Although the latter method is observationally and computationally burdensome, fewer assumptions need to be made. Both methods have produced accretion disk temperature profiles consistent with the thin disk model of Shakura & Sunyaev (1973), though observed disk sizes tend to be larger than the Shakura & Sunyaev (1973) simple thin disk model (Morgan et al., 2010).

In this paper we present an analysis of the uncorrelated variability in the light curves of the quadruply lensed quasar WFI J2033-4723. In §2 we present a broad discussion of the properties of quasars and lensing phenomena, and we describe the particular system we analyzed. We describe the observational data in §3, and in §4 we provide a more detailed examination of the microlensing technique we employed to obtain parameters of interest. Then, in §5 we present and comment on the results obtained from our microlensing analysis. Finally, we examine the implications of our results for correlations between luminosity, accretion disk size, and black hole mass in §6. We maintain a flat cosmology with $\Omega_M = 0.3$, $\Omega_\Lambda = 0.7$, and $H_0 = 70 \text{ km s}^{-1} \text{ Mpc}^{-1}$ (Hinshaw et al., 2009) for this paper.

2. Background

2.1. Description of Observational Properties

The most prominent characteristics of quasars are their prodigious luminosities and broad spectral energy distributions (SED). To first order, stars radiate like blackbodies (which are characterized by an emission spectrum that peaks at only one wavelength and falls off quickly at other wavelengths) at a temperature corresponding to the star's surface temperature, but as we show in Figure 1, quasars radiate across the entire electromagnetic spectrum.

We see from Figure 1 that the spectral energy distribution is profoundly non-stellar due to emission at all wavelengths. Another defining characteristic of quasars is the variability of their brightness. They are variable at every wavelength, not only in the continuum, but also in their broad emission lines (Peterson, 1997; Bentz et al., 2006). The luminosity of many quasars varies by factors of two or even five on timescales of weeks or months. Some have been found to vary significantly over the course of a few days.

We know very little about the physical structure of the central engine in quasars because their angular size (an objects apparent size as seen by an observer on Earth) is

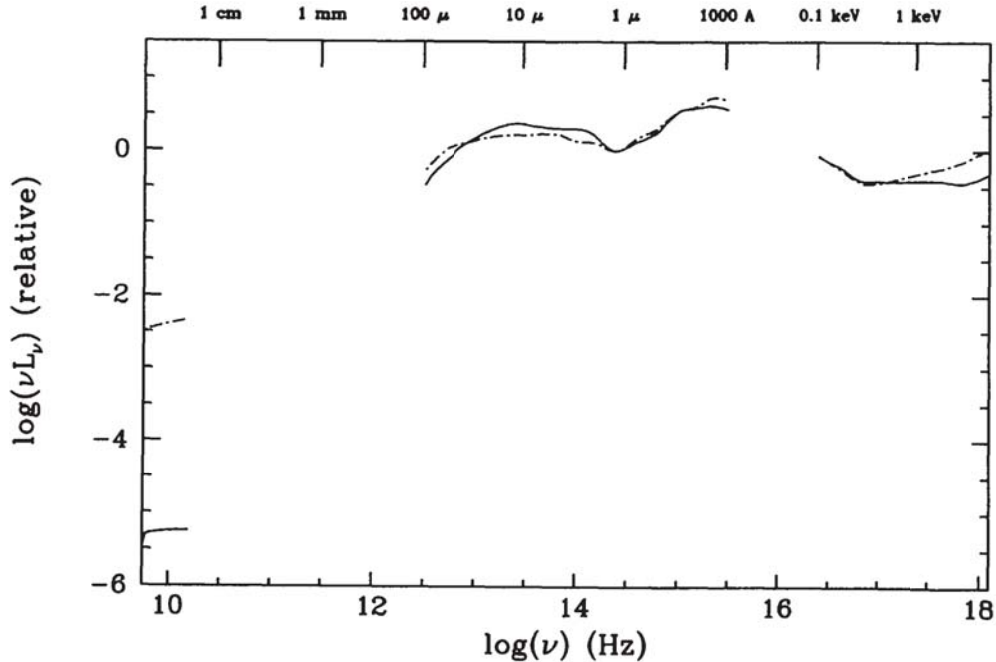


Fig. 1.—: Mean spectral energy distributions for a sample of radio-quiet and radio-loud quasars (Elvis et al., 1994). L_ν is the specific luminosity (per unit frequency interval), ν is the frequency and the luminosity scale has been arbitrarily normalized at a wavelength of $1\mu\text{m}$ (Peterson, 1997).

so small. According to Rayleigh's criterion the minimum angle that can be resolved by a circular aperture of diameter D is

$$\alpha = 1.22 \frac{\lambda}{D} \quad (1)$$

where α is the angular resolution measured in radians, λ is the wavelength of light observed, and D is the diameter of the circular aperture of a telescope. Since quasars are billions of light years away, their angular sizes α are extremely small. We currently lack the means to resolve them with even the largest optical telescopes. The level of angular resolution that would be required is similar to that needed to resolve sand grains on the moon.

2.2. Model for the Source of the Continuum Emission: SMBH Accretion

Since their discovery (Schmidt, 1963), there have been significant attempts to understand the source that powers the quasar central engine. The leading model today is accretion onto a super massive black hole (SMBH) leading to the continuum emission observed in the spectra of quasars. As matter spirals in towards the black hole, it forms a disk which is heated by dynamical friction to temperatures greater than 10^5 K. This is believed to be the source of the strong continuum emission seen in quasar spectra. Although there are newer and more complex theoretical alternatives (e.g. Page & Thorne, 1974; Hubeny & Hubeny, 1997; Hubeny et al., 2001; Li et al., 2005; Narayan, Barret & McClintock, 1997; De Villiers, Hawley & Krolik, 2003; Blaes, 2007) , the simple Shakura & Sunyaev (1973) thin disk model remains the standard model for accretion disk emissivity because we do not have sufficient observational evidence to change it. The Shakura & Sunyaev (1973) thin disk model is an optically thick disk with a temperature profile that is hotter in the middle and cooler on the outer edges. Each annular ring emits as a blackbody at its own different temperature, resulting in a $T \propto R^{-\frac{3}{4}}$ temperature profile, where R is the radial position in the disk. Moreover, since we assume that each ring radiates as a blackbody, the surface brightness f_ν at rest wavelength ν and radial position R is given by

$$f_\nu = \frac{2h_p c}{\lambda_{rest}^3} (\exp(\frac{R}{R_{\lambda_{rest}}})^{\frac{3}{4}} - 1)^{-1} \quad (2)$$

where the scale length $R_{\lambda_{rest}}$ is the the radius at which the disk temperature matches the wavelength, $kT_{\lambda_{rest}} = \frac{h_p c}{\lambda_{rest}}$ (Morgan et al., 2010).

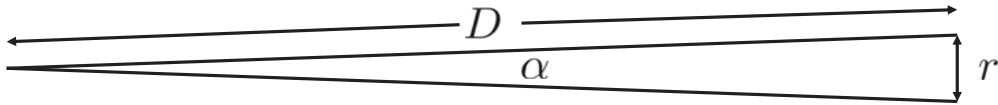


Fig. 2.—: Diagram of angular size where D in this case is the distance to the quasar, r is the physical size of the quasar and α is the angular size.

The Shakura & Sunyaev (1973) thin disk model can be used to explain many of the observational features of the quasar SED, but until very recently there were no physical tests of the scales because a typical quasar accretion disk is of microarcsecond (μas) angular size and hence cannot be resolved with ordinary telescopes. Fortunately, a phenomenon known as gravitational lensing has given us the necessary resolution to study the structure of the quasar continuum source.

2.3. Introduction to Gravitational Lensing

General Relativity predicts that the trajectory of photons (light rays) will be affected as they pass by massive objects, much as the path of a space probe would be deflected as it passed by a planet (Einstein, 1916). This phenomenon allows for the mechanism of a gravitational lens; a system in which the light emitted by a distant object is deflected by the mass located between the object and the observer. There are three main components to a gravitationally lensed quasar. There is the source (the quasar), the lens (the lensing galaxy), and the observer (us). The basic setup is shown in the left panel of Figure 3. Light rays emitted by the source are deflected by the lens. For a point-like lens, there will always be at least two images of the source. Furthermore, with external shear due to the gravitational interactions of objects outside but near the light bundles, there can be even more images (Wambsganss, 1998).

In the special case when the source lies exactly behind the lens, a ring-like image, a so called “Einstein Ring”, occurs with angular radius R_{Ein} . Real lenses are never perfectly aligned or symmetric, but occasionally they come close.

Another effect of gravitational lensing is “time delays”. Time delays are the difference in the light travel time between the two images as seen by the observer. Time delays are a function of the image geometry, the gravitational potential of the lensing galaxy, the distance to the lens from the observer, the distance to the source from the observer, and the distance from the lens to the source (Wambsganss, 1998). There are two components that make up a time delay. The first is geometric; the light emitted by the source has to travel an additional distance compared to a direct line between the observer and the source. Moreover, the path lengths for the individual images are different so there is a difference in time between the arrival of light from different images of the source. The other component is gravitational; the gravitational potential of the mass of the lensing galaxy retards time in the individual images as predicted by Einstein’s Theory of General Relativity .

There is another lensing phenomenon known as “microlensing”. To this point we have described the phenomenon of “strong” lensing in which the positions of the images and their magnification is caused by the galaxy as a whole. When the separation between images is not large enough to avoid interference with the lensing galaxy, photons from the quasar pass through the disk of the lens galaxy which contains stars and possibly

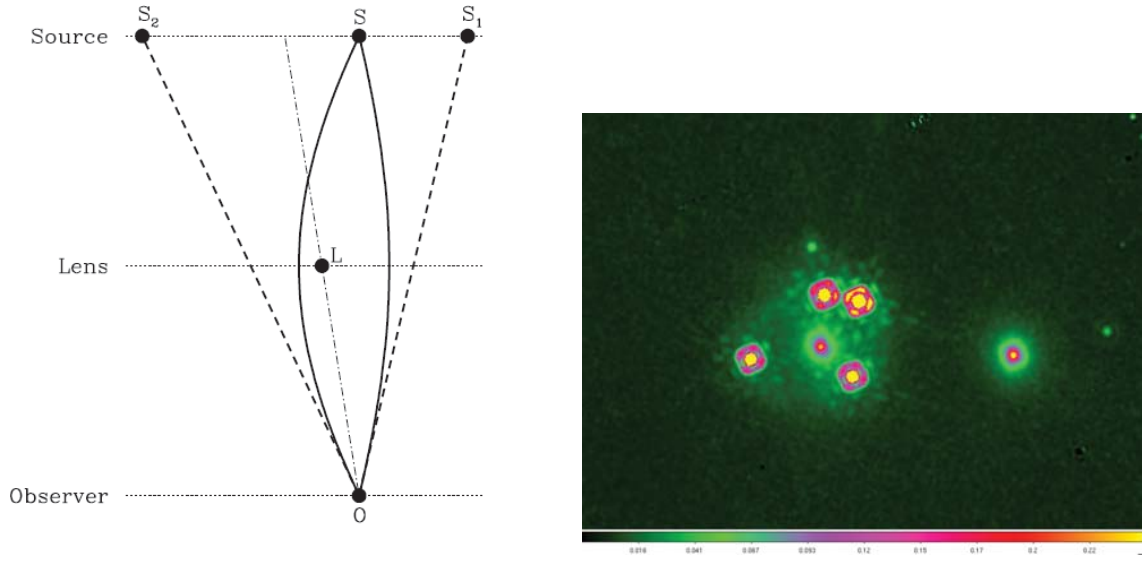


Fig. 3.—: Left: Diagram of a gravitational lens in which the lens L produces two images S_1 and S_2 of the source S that are seen by the observer O (Wambsganss, 1998) Right: In this infrared (H-band) image taken by NASA's Hubble Space Telescope, the quasar WFI J2033-4723 is quadruply imaged due to the gravitational lens made by the lensing galaxy . The four bright point sources are the quasar and the lensing galaxy is in the center of the four bright point sources. The point on the right (west) of the frame is a neighboring galaxy that was included in our lens modeling.

compact objects. Passage by individual stars will also cause deflection of the light rays, but the angular deflections are much smaller in this case, so multiple images cannot be detected. Passage by a star may lead to temporary magnification (or demagnification) of a ray, however. As they pass through the lens galaxy, the light rays will encounter many individual “microlenses”, which, when projected onto the source plane yield a complicated two-dimensional magnification like that in Figure 4 (Wambsganss, 1998). Since there is relative motion between observer, lens and source, the quasar changes its position relative to this magnification pattern, and so the apparent brightness of the quasar changes with time (Wambsganss, 1998). When the objects in the lensing galaxy have Einstein radii (R_{Ein}) of approximately the same size or larger than the size of the quasar source, they can cause noticeable magnifications in an image (e.g. Morgan et al., 2006). Since the period and magnitude of the magnifications are dependent upon the size of the source, this signal can be exploited to examine the structure of quasars. Moreover, we can extract important information about the lensing galaxy itself from the microlensing magnifications (Schechter & Wambsganss, 2002).

Many different factors affect quasar microlensing, however, so extracting information about a quasar’s structure and its lens galaxy is non-trivial. First, we have to account for the characteristics of the lens galaxy including the surface mass density, average stellar mass, magnification and shear at the location of each image, the stellar velocity dispersion, and the total velocity of the lens galaxy (Kochanek, 2004). We also have to estimate an effective source velocity. Since there is a wide range of values for each of the different parameters, namely effective velocity, source size, and the physical conditions in the lensing galaxy that yield the magnification patterns, we use Monte Carlo methods to marginalize over these unknown parameters (Kochanek, 2004). In this technique, a range of model sources are run past a large set of model microlensing magnification patterns on a large number of random trajectories and velocities in an attempt to recreate the observed data. Trials that produce good fits to the data are given more statistical weight. The result is a set of probability distributions for the parameters of interest.

2.4. Introduction to WFI 2033-4723

The quadruply-lensed quasar WFI J2033-4723 (hereafter WFI 2033; $20^h33^m42.08^s$, $-47^\circ23'43.0''$ [J2000.0]) was discovered during a wide-field imaging survey for lensed quasars in the southern hemisphere using the MPG/ESO 2.2 m telescope (Morgan et al., 2004). It has redshift of $z = 1.66$ and a maximum image separation of 2.5 arcseconds (Morgan et al., 2004). Vuissoz et al. (2008) measured a time delay of $\Delta t_{B-A} = 35.5 \pm 1.4$ days and $\Delta t_{B-C} = 62.6^{+4.1}_{-2.3}$ days between the appearance of the quasar’s intrinsic variability in the multiple images.

Two teams began monitoring WFI 2033 shortly after its discovery in 2004: a Swiss

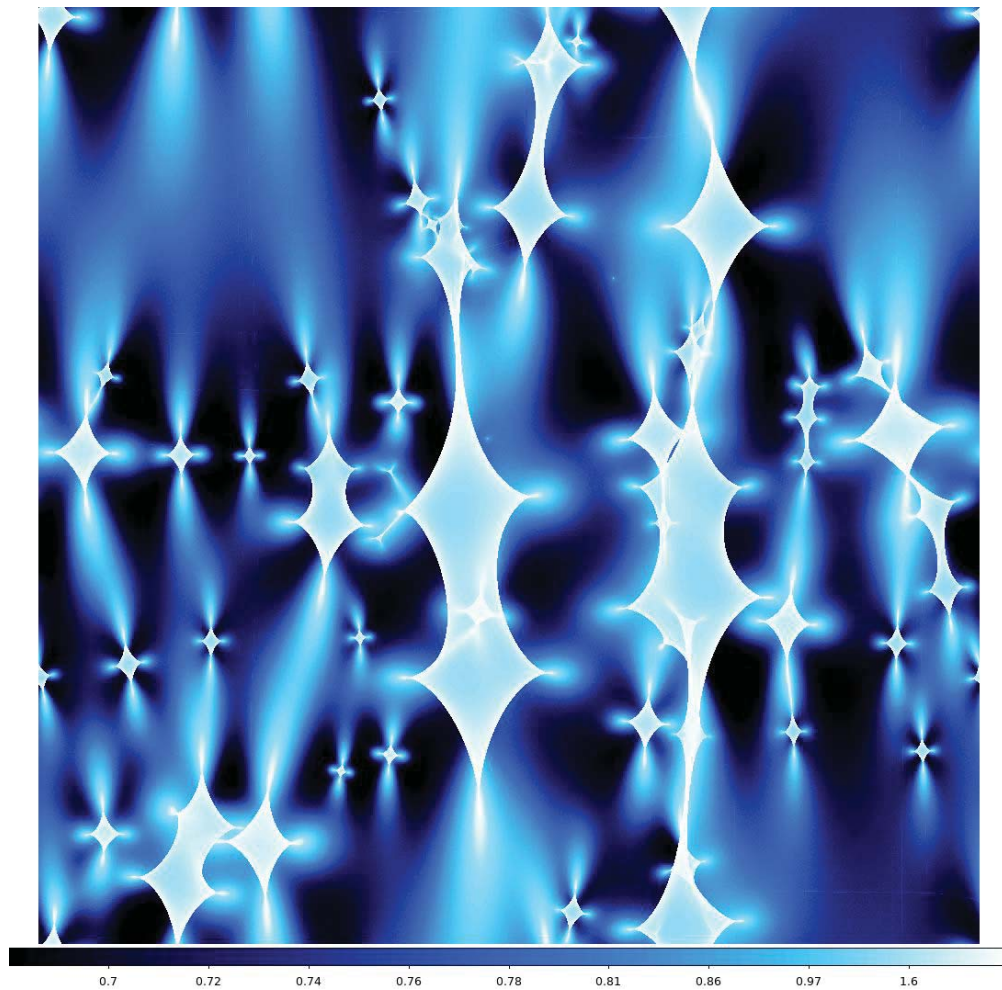


Fig. 4.—: Magnification pattern in the source plane, produced by a dense field of stars in the lensing galaxy. The color reflects the magnification as a function of the quasar position: the sequence black-dark blue-light blue-white indicates increasing magnification. The microlensing parameters were chosen according to a model for image A1 of the quadruple quasar WFI J2033-4723.

group using the 1.2 m EULER¹ telescope in Chile at La Silla and an American group using the 1.3 m telescope of the Small and Moderate Aperture Research Telescope System (SMARTS)² in Chile at the Cerro Tololo Interamerican Observatory (CTIO). Data from this monitoring campaign was used by Vuissoz et al. (2008) to measure the time delay between the appearance of intrinsic variability in the images of the lensed quasar, but both groups have continued to take regular *R*-band optical images. Per a pre-existing collaboration agreement with the Swiss group of Dr. Frederic Courbin at the Ecole Polytechnique Federale de Lausanne and Dr. Chris Kochanek at The Ohio State University, the raw images from both the EULER and SMARTS telescopes were transferred to computers at the U.S. Naval Academy.

Figure 5 shows the optical spectrum of WFI 2033 (Morgan et al., 2004). This system's redshift was measured by comparing the rest-frame wavelength of the Mg II, C III, and C IV emission lines to the observed values. The redshift z is given by

$$1 + z = \frac{\lambda_{observed}}{\lambda_{emitted}} \quad (3)$$

where $\frac{\lambda_{observed}}{\lambda_{emitted}}$ is the ratio of the light's wavelength as measured by the observer and its wavelength when it was emitted from the distant object.

3. Observations and Data Reduction

The camera used for the 1.3 m SMARTS telescope was the dual-beam ANDICAM instrument (DePoy et al., 2003). For this study we used the optical channel which has a plate scale of 0".369 per pixel and a field of view of 6.5'x6.3'. The average sampling of the SMARTS data is one epoch every eight days, with six 300 s exposures at each epoch using the *R*-band filter. The *R*-band filter has an effective wavelength of 658 nm translating to a rest-frame wavelength of 247 nm which is in the UV region (see equation 3).

The camera used for the 1.2 m EULER telescope was the 4096x4112 EulerCAM camera which has a plate scale of 0".2149 per pixel and a field of view of 15'x15'. The average sampling of the EULER data is one epoch every five days, with five 360s exposures at each epoch using a 'RG' or 'Rouge Genève' filter. The RG filter is a modified broad Gunn *R* filter, with an effective wavelength of 660 nm translating to a rest-frame wavelength of 248 nm. The EULER dataset consists of 266 epochs between October 2010 and December 2016.

In Figure 6, we display an image of WFI 2033 taken with the 1.3 m SMARTS telescope next to an image of that same system taken above earth's atmosphere using the Hubble

¹<http://www.eso.org/public/usa/teles-instr/lasilla/swiss/>

²<http://www.astro.yale.edu/smarts/1.3m.html>

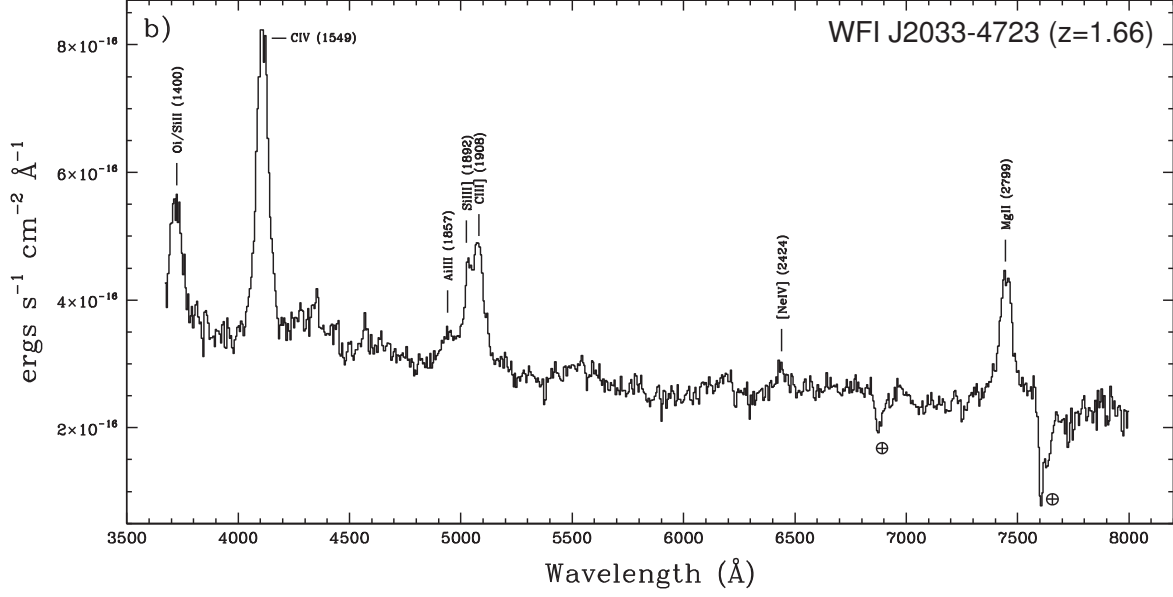


Fig. 5.—: Unresolved long-slit spectrum obtained with the CTIO 1.5 m. The continuum emission is the relatively flat space between the labeled emission lines.(Morgan et al., 2004)

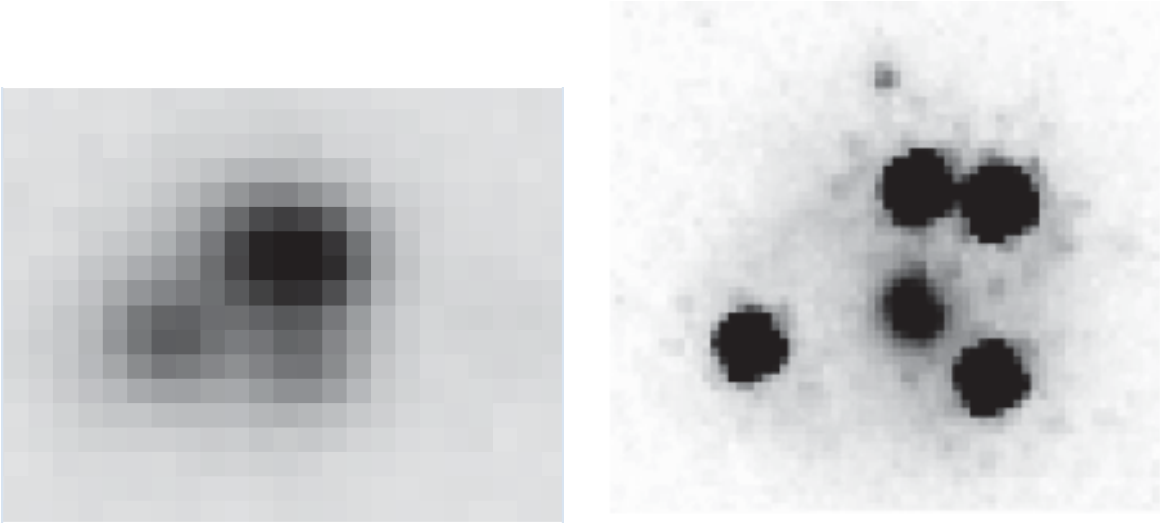


Fig. 6.—: Left: Result of a processed yet undeconvolved SMARTS image of WFI J2033–4723. Right: a deep NICMOS2 image, taken in the F160W-band using *HST*. This image had a total exposure time of 46 min after combining 4 frames. North is up and East to the left (Vuissoz et al., 2008).

Space Telescope (*HST*). Since the atmosphere blurs the system's multiple images such that they overlap with each other and the lens galaxy, measuring the brightness of each component is a challenge. We employed a technique known as “point spread function” (PSF) modeling in which the atmosphere’s influence on the light from a point source is first modeled by analyzing the distribution of light in selected isolated stars in the frame (see Figure 7). This PSF model was then applied to the blended quasar images, allowing for an independent measurement of the brightness of each image. We also stacked the individual images from each night to improve the signal-to-noise ratio. Plotting the brightness of each image in WFI 2033 over the course of many nights created a set of “light curves”.

After using the PSF modeling software to assemble the light curves and applying subsequent seeing cuts, we needed to combine the two light curves together. Since the SMARTS and EULER telescopes each have their own detectors with their own quantum efficiencies and slightly different filters, a small color term between the different datasets affects our relative photometry measurements. We calculated this color term by fitting the light curves obtained with the ANDICAM instrument to those obtained from the EulerCAM camera, yielding a magnitude offset of $m_{ANDICAM} - m_{EulerCAM} = 0.0087$ mag. We apply this correction to the SMARTs data.

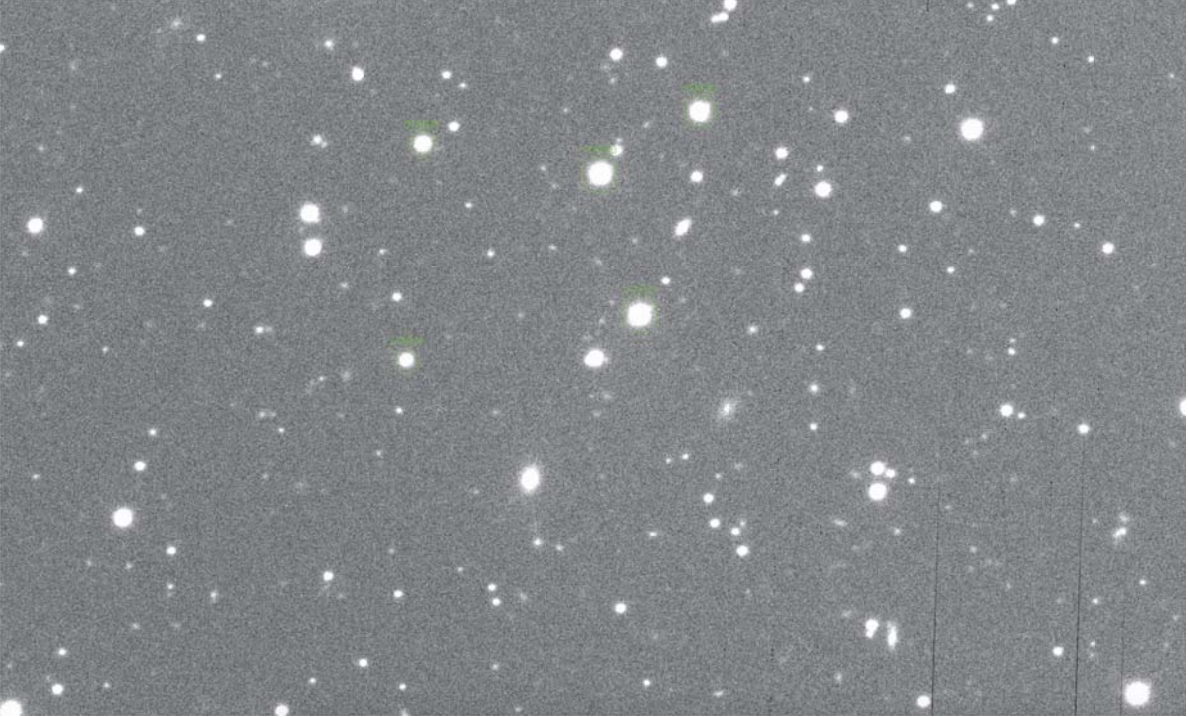


Fig. 7.—: Image of WFI 2033 in its environment taken with the EULER telescope. The reference stars are circled in green and WFI 2033 is centered on the frame, adjacent to STAR20.

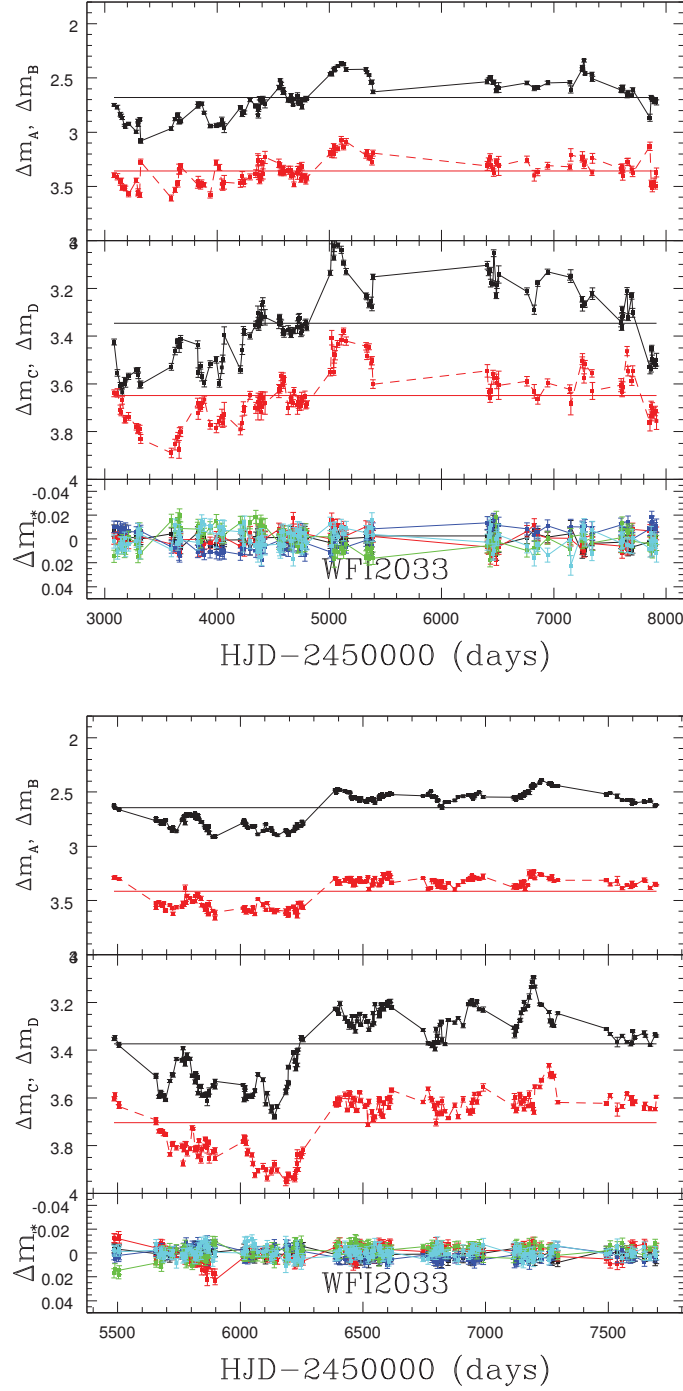


Fig. 8.—: Top: R-band light curve of WFI 2033 from SMARTS after a $1''.5$ seeing cut. Bottom: R-band light curve obtained for WFI 2033 as from EULER after a $1''.62$ seeing cut. The magnitudes are given in relative units. The bottom panel, Δm_{star} shows the brightness of the reference stars plotted relative to their mean from all epochs.

Next we binned our light curves using a window of twenty days to further improve the signal to noise ratio. The twenty day binning window was sufficiently short to avoid overly smoothing the microlensing variability while allowing for an improved signal to noise ratio. The date of each twenty-day bin was set as the mean Heliocentric Julian Day (HJD) of the measurements included in that bin. For the errors on these twenty-day averages, we used the standard deviation of the mean to reduce the aggregated uncertainties by a factor of \sqrt{N} where N is the number of nights of observation in the twenty-day bin. In the final stages of analyzing the data, we decided to remove the last 5 seasons of SMARTS data. Marginal observing conditions and instrument variability lead to a consistently unstable point spread function in the SMARTS data, rendering those flux measurements too noisy to use. We show the final composite light curves for WFI 2033 from both of the data sources in Figure 9, and we provide full tables of all of the brightness measurements in Appendix A.

4. Microlensing Analysis

When analyzing light curves for the presence of microlensing variability, it is important to first eliminate the variability that is intrinsic to the source itself. Fortunately, the time delays for WFI J2033-4723 were measured by Vuissoz et al. (2008). When we offset our light curves by the measured time delays and divide one of the light curves by another, only variability due to extrinsic effects along the line of sight (viz. microlensing) will remain. See Figure 9 for an example of this process.

In essence, our Bayesian Monte Carlo technique is an attempt to reproduce the observed microlensing variability using a range of very realistic models for the physical conditions that might have led to this variability. All of this hinges on our ability to accurately model the conditions in the lens galaxy through which the quasar’s light must pass. We started by applying the LENSModel code of Keeton (2001) to the very precise astrometry (positions) and photometry (brightness) provided by the *HST* observations to yield a range of physically plausible models for the stellar and dark matter content in the lens galaxy at the positions of the lensed images. These lensing galaxy models consisted of a combination of a de Vaucouleurs profile for the luminous matter and a Navarro-Frenk-White (NFW) (Navarro, Frenk & White, 1996) profile for the dark matter halo. We created 10 models of the lensing galaxy. The first was entirely luminous matter, the second had 10% of its total mass as dark matter, the third had 20% dark matter, and so on up to 90% dark matter. Our model also included the convergence and shear from a galaxy at similar redshift as the lens, located to the west of the lens galaxy in our simulations (See the right panel of Figure 3). We modeled this local galaxy as a single isothermal sphere (SIS) in our models because it is close (4 arcseconds) and of similar luminosity to the lensing galaxy (Vuissoz et al., 2008). These models were judged by how well they reproduced the *HST* astrometry within strict parameters. See Table 1 for the specific ingredients of the different lens galaxy mass models. When a model diverged from the parameters, it was assigned a χ^2

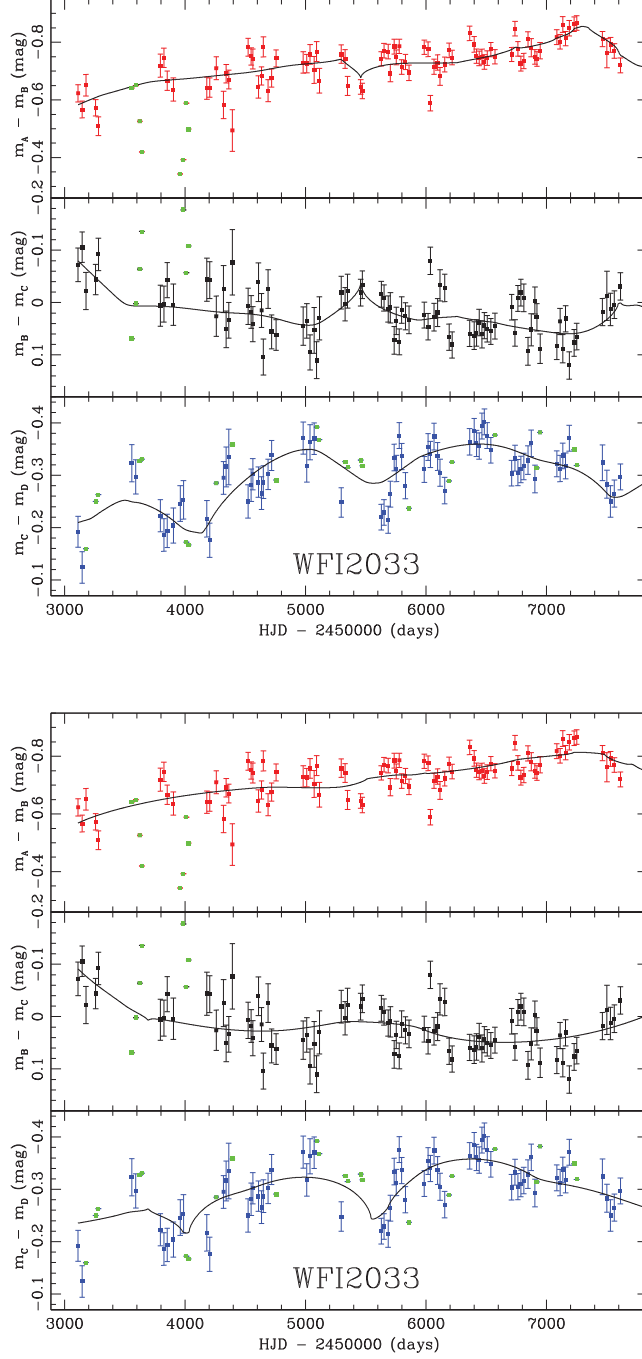


Fig. 9.—: Time delay corrected difference light curves: The raw combined EULER and SMARTS light curves were shifted by the measured time delays, binned into twenty day windows, and then subtracted from each other. The curves represent the best fits from our Monte Carlo Analysis. The green points represent data we excluded from the fit due to inter-seasonal extrapolation beyond our set threshold of 20 days. Over the course of 13 seasons we see $\Delta m_{ab} \approx \Delta m_{bc} \approx 0.2$ of microlensing variability.

penalty. From these models, we generated a large number of microlensing “magnification patterns”, exploiting the inverse ray-shooting technique (e.g. Wambsganss (1998)) on the USNA high-performance computing cluster. See Figure 4 for an example of a microlensing magnification pattern.

For each of our macro models parameterized by dark matter content, we generated forty random realizations of the expected microlensing magnification patterns for each image. We modeled the accretion disk of the quasar as a standard, face-on thin disk model (Shakura & Sunyaev, 1973) with a scale length of $\hat{r}_s = r_s / \langle M / M_\odot \rangle^{1/2}$ where $\langle M \rangle$ is the mean mass of a star in the lens galaxy. For the analysis of the combined Euler and SMARTS light curves we used the Monte Carlo method of Kochanek (2004). This involved randomly generating 40 billion trial light curves and fitting them to the observed light curves. We quantified the quality of these fits using the χ^2 metric, and we assessed the resulting distributions of χ^2 values using Bayesian statistical methods to acquire probability distributions for the model parameters. For each realization of this process we randomly choose an initial position and trajectory for the source, assuming these values are independent and uniformly distributed. Next, we fit the trial light curve to the observed data and assessed the quality of the fit using the χ^2 statistic. Runs that were awarded a χ^2 value greater than a pre-imposed limit were automatically discarded because they contributed negligible statistical weight to the solution. See Figure 9 for examples of two good trial light curve fits to the observed data.

To properly account for the effects of the finite quasar source, we first convolved the magnification patterns with the surface brightness profile of the source for a range of different source sizes prior to making the trial light curves. We modeled the source as a face-on thin disk with a $T \propto R^{-3/4}$ temperature profile as described in §2.2. However, since we modeled the disk as a face-on disk, its radius is only the radius of the projected area of the accretion disk. Therefore, we corrected this radius by a factor of $(\cos i)^{-1/2}$ where i is the inclination of the disk from face on. Then we traced a single point through the convolved magnification pattern to generate a trial light curve.

Once the run was complete, we employed Bayesian methods to analyze the χ^2 statistics of the different light curve fits which yielded the probability densities for the quasar source size and velocity in Einstein units (\hat{r}_s and \hat{v}_e). Using Bayes’ theorem, the probability of the parameters given the data D is

$$P(\xi_p, \xi_t | D) \propto P(D | \xi_p, \xi_t) P(\xi_p) P(\xi_t), \quad (4)$$

where ξ_p is the collection of physical variables, ξ_t is the collection of trajectory variables and therefore, $P(\xi_t)$ and $P(\xi_p)$ are the estimates of the prior probabilities for the trajectory and physical variables respectively. The physical variables are the collection of local magnification tensors (mean convergence κ and mean shear γ), the local properties of the stars (surface density of stars κ_\star , mass of the average microlens $\langle M \rangle$, and parameters of the distribution of microlens masses x and r), the structure of the source (r_s), and the effective velocity of the source (\vec{v}_e). The distribution of microlens masses is given by an

$f_{M/L}$	Convergence κ				Shear γ				κ_*/κ			
	A1	A2	B	C	A1	A2	B	C	A1	A2	B	C
0.1	0.75	0.83	0.61	0.92	0.13	0.30	0.15	0.27	0.014	0.025	0.010	0.031
0.2	0.71	0.80	0.57	0.89	0.15	0.35	0.15	0.33	0.029	0.051	0.021	0.063
0.3	0.68	0.76	0.53	0.85	0.17	0.40	0.15	0.39	0.046	0.079	0.033	0.097
0.4	0.65	0.72	0.50	0.82	0.18	0.45	0.16	0.45	0.07	0.11	0.05	0.14
0.5	0.61	0.68	0.45	0.78	0.20	0.51	0.16	0.51	0.09	0.16	0.07	0.19
0.6	0.58	0.64	0.42	0.75	0.22	0.56	0.17	0.57	0.11	0.19	0.08	0.22
0.7	0.54	0.60	0.37	0.70	0.24	0.63	0.17	0.64	0.16	0.27	0.13	0.30
0.8	0.50	0.56	0.33	0.67	0.26	0.68	0.18	0.69	0.19	0.32	0.16	0.35
0.9	0.45	0.51	0.27	0.63	0.28	0.76	0.19	0.77	0.29	0.47	0.27	0.49
1.0	0.43	0.48	0.26	0.60	0.29	0.78	0.19	0.81	0.27	0.46	0.25	0.48

Note. — Convergence κ , shear γ and the fraction of the total surface density composed of stars κ_*/κ at each image location for the series of macroscopic mass models where $f_{M/L} = 1.0$ corresponds to a constant mass-to-light ratio model for the lens galaxy.

Table 1. WFI2033–4723 Lens Galaxy Mass Models

empirical function that describes the initial masses for a population of stars when they first begin hydrogen fusion. This power law mass function $\frac{dp}{dM} \propto M^{-x}$ over a finite mass range of $M_1 < M < M_2$ is parametrized by x along with the ratio between the upper mass and lower mass $r = \frac{M_2}{M_1}$. In our calculations we used a Salpeter initial mass function (IMF) which is characterized by a parameterization of $x = 2.35$. For any particular combination of physical parameters we also produced a large set of source trajectories with different starting points and directions. We treated these trajectory variables as nuisance parameters since we assumed they were independent and uniformly distributed. We marginalized over the nuisance variables to find the probability distribution for the more interesting statistical parameters giving us

$$P(\xi_p|D) \propto \int P(\xi_p, \xi_t|D)d\xi_t, \quad (5)$$

where the Bayesian parameter estimates were normalized such that the total probability is unity, $\int d\xi_p d\xi_t P(\xi_p, \xi_t|D) = 1$ (Kochanek, 2004). As long as the trajectory variables are uniformly distributed and there is a large number of trials, the sum of the random trajectories will converge to the integral above.

Extrinsic variability due to microlensing will be significant if the characteristic source size r_S is less than the Einstein radius of the microlenses, r_E . Smaller ratios of r_S/r_E will lead to larger amplitudes of microlensing fluctuations. The timescales for microlensing variability are determined by the characteristic times $t_E = r_E/v$ and $t_S = r_S/v$ where v is the effective transverse velocity of the source. If r_S is indeed smaller than r_E , microlensing events will roughly take place on a timescale of $t_E = r_E/v$, which is the time it takes the source to move across the Einstein radius of a $1M_\odot$ star. On the other hand if the source is small and moving through a busy region in the microlensing magnification pattern, microlensing variability will have a shorter timescale, namely $t_S = r_S/v$, which is approximately the time it takes the source to move across its own diameter.

The effective velocity of the source is composed of three elements: the motion of the observer, the lens, and the source (Kayser et al., 1986). In order to define the probability density of effective source velocities ($\frac{dP}{dV_e}$) we must first separate the various terms into Gaussian and fixed components, following the method of Kochanek (2004). The unknown components are the peculiar velocities of the of the lens and the source. Treating them as Gaussian distributed variables and summing them in quadrature we have a one-dimensional source plane velocity dispersion of

$$\sigma_e^2 = \left[\frac{\sigma_{pec}(z_l)}{1+z_l} \frac{D_{OS}}{D_{OL}} \right]^2 + \left[\frac{\sigma_{pec}(z_s)}{1+z_s} \right]^2 \quad (6)$$

where $\sigma_{pec}(z)$ is the the one-dimensional root mean square (rms) galaxy peculiar velocity at redshift z . D_{OS} and D_{OL} are the angular diameter distances between the observer and source and the observer and lens respectively. We used a peculiar velocity of 275 km s^{-1} for the lensing galaxy.

The projection of the cosmic microwave background (CMB) velocity onto the source

plane and the stellar velocity dispersion are assumed to be constant and we sum these components in quadrature to yield a typical velocity of

$$\bar{v}_e^2 = \left(\frac{v_{CMB}}{1+z_l} \frac{D_{LS}}{D_{OL}}\right)^2 + 2\left(\frac{\epsilon\sigma_*}{1+z_l} \frac{D_{OS}}{D_{OL}}\right)^2 \quad (7)$$

where v_{CMB} is the projection of the CMB dipole velocity (Hinshaw et al., 2009) onto the lens plane, and σ_* is the velocity dispersion of the stars in the lens galaxy. We used a one dimensional stellar velocity dispersion in the lens galaxy of 366 km s^{-1} . The cosmic microwave background radiation is the afterglow of the Big Bang, and since it is isotropic, the peculiar motion of the Sun (i.e., the motion that is not due to the Hubble flow) causes an observable dipolar Doppler shift in the background that permits a measurement of the observer's velocity relative to the local universe. For our velocity model we used the projected velocity of the cosmic microwave background dipole onto the plane of lens of -234 km s^{-1} east and $-235.504 \text{ km s}^{-1}$ north as the observer's transverse velocity.

Combining the the Gaussian and fixed components we obtain the the rms source velocity of

$$\langle v_e^2 \rangle^{1/2} = (\sigma_e^2 + \bar{v}_e^2)^{1/2}. \quad (8)$$

We assumed a 0.017 magnitude systematic uncertainty in the photometry of the individual images. With this assumption we generated the 40 billion trial light curves for each mass model, magnification pattern and source size, with a best fit $\chi_{best}^2/N_{dof} \approx 1.9$. To convert the results from Einstein units where all physical scales depend on the on the mean mass of the microlenses $\langle M/M_\odot \rangle$, we have to assume a prior for the mean stellar mass. To this end, we created a probability density for the average stellar mass in the lensing galaxy from Figure 10a since $\langle M \rangle$ is related to \hat{v}_e and v_e by $\hat{v}_e \propto v_e/\langle M \rangle^{1/2}$. We show the result for the lens-galaxy stellar mass estimate in Figure 10b.

When we convolve the probability densities in Figure 10b and Figure 10c, the result is a preliminary probability density for the quasar's scale radius in physical units

$$\frac{dP}{dr_s} = \int_0^\infty \frac{dP}{d\langle M \rangle} \frac{dP}{d\hat{r}_s} d\langle M \rangle, \quad (9)$$

but we can generalize this process to any variable of interest in the simulation.

5. Results and Discussion

5.1. Results

In Figure 10a we display the probability distribution for the effective source plane velocity \hat{v}_e (which we obtained from the Bayesian analysis of our Monte Carlo code simulations) as compared to the unscaled, true source plane effective velocity which we

obtained through the methods described in §4. The \hat{v}_e distribution has a median of 14000 km s⁻¹ with a 68% confidence range of 8000 km s⁻¹ < \hat{v}_e < 23000 km s⁻¹. Dividing the unscaled effective source velocity distribution by the scaled effective velocity distribution we obtain the probability distribution for the mean microlens mass $\langle M \rangle$ seen in Figure 10b since $\hat{v}_e = v_e / \langle M / M_\odot \rangle^{1/2}$. In Figure 10c we show that we were able to constrain the effective source size in Einstein units; note that the probability density is converging at one value. Although the scaled effective source plane velocity and mean stellar mass distributions are clearly non-physical, this can be explained by the degeneracy between the microlens mass and effective source plane velocity. This degeneracy is demonstrated in Figure 10d where we show that the relative probability distribution for the physical thin disk scale size r_s from our microlensing simulations is consistent with the result of imposing a uniform prior on the mean microlens mass of $0.1 \leq \langle M / M_\odot \rangle \leq 1.0$.

We have every reason to believe that the true median stellar mass is between 0.1 and 1 M_\odot , but we have no way to measure it directly. When applying this prior, our results should be identical to the results where all solutions are equally likely. We find a non-inclination corrected physical source size of $\log(r_s/\text{cm}) = 15.9 \pm 0.3$ without the prior applied and one of $\log(r_s/\text{cm}) = 16.0_{-0.6}^{+0.2}$ with it applied. The consistency of these two probability distributions confirms the validity of our results.

5.2. Discussion

Although Vuissoz (2008) found no evidence for microlensing variability over a time scale of three years (March 2004 to May 2007), we can confidently report the presence of microlensing variability in our longer observational window. We believed longer term microlensing might have been present because the flux ratios found by Vuissoz et al. (2008) did not agree with those measured in the quasar emission lines (Morgan et al., 2004). There are several reasons why the microlensing may appear to be quasi-static. The source could be very large such that the lensing stars in the foreground would only be able to microlens a small region of the source at a time, making the microlensing variability hard to detect. Alternatively, there might be a low relative transverse velocity between the lens, observer, and source.

Motta et al. (2017) measured a black hole mass of $M_{BH} = 1.2_{-0.8}^{+3.1} \times 10^8 M_\odot$ using the C III] emission line. Applying the Accretion Disk Size - Black Hole Mass relation of Morgan et al. (2010) we would predict an accretion disk size of 1.1×10^{15} cm in WFI 2033. We expect our measurement to be larger than that predicted by Shakura & Sunyaev (1973), who made the assumption that the quasar accretion disk is a physically thin but optically thick system. However, since every accretion disk measured, including that of QJ0158–4325 in Morgan et al. (2008), is larger than that predicted by Shakura & Sunyaev (1973), accretion disks must not be as efficient as the theoretical model would predict. Instead, to compensate for their relative inefficiency, they must be bigger to produce the

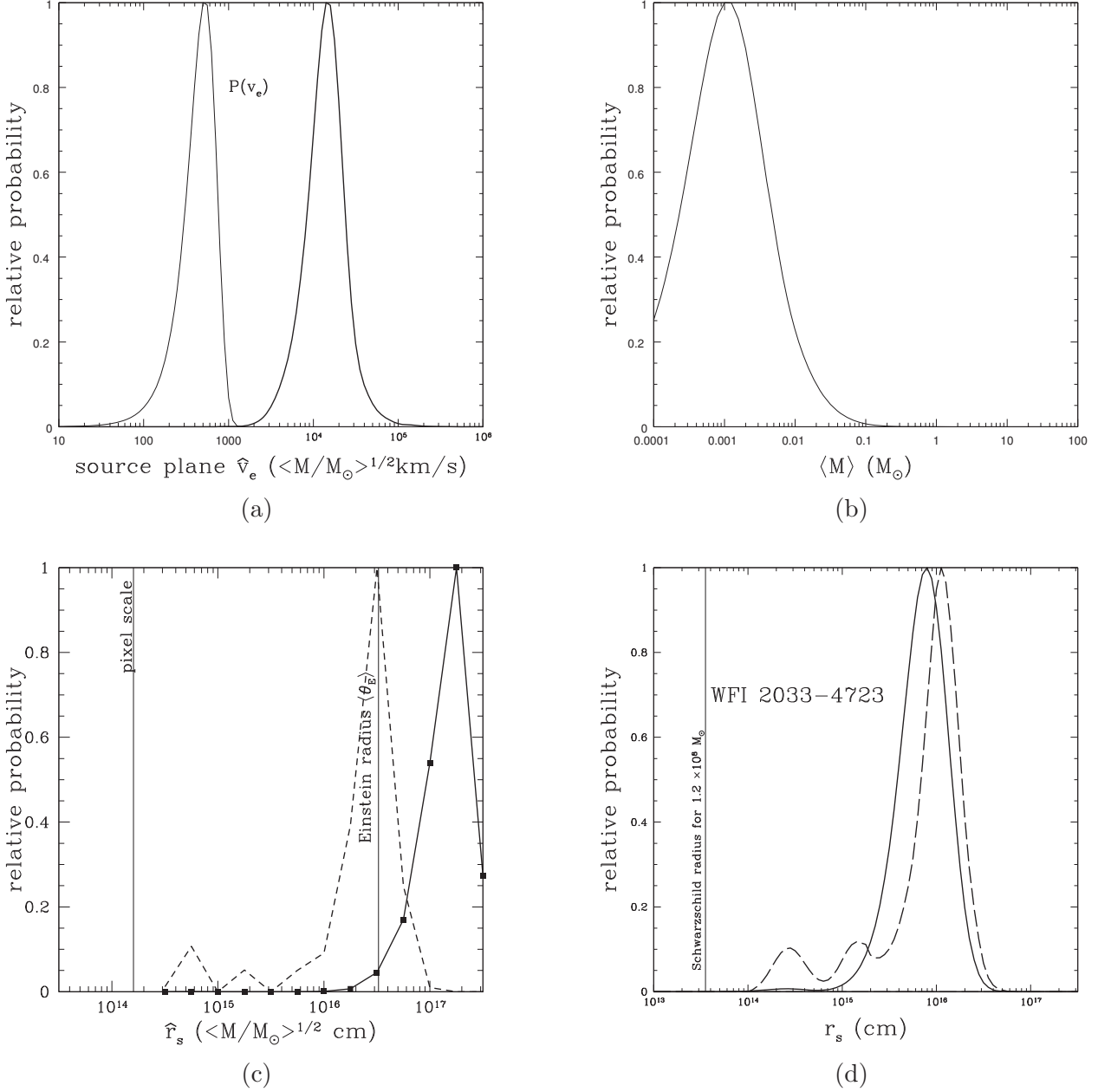


Fig. 10.—: (a) Probability density for the effective source plane velocity \hat{v}_e (*heavy solid line*) as compared to our estimated probability distribution for the true source plane effective velocity v_e (*light solid line*). The average microlens mass $\langle M \rangle$ is related to \hat{v}_e and v_e by $\hat{v}_e = v_e / \langle M/M_\odot \rangle^{1/2}$. Consequently, the high (low) ratios of \hat{v}_e/v_e correspond to low- (high-) mass microlenses. (b) Probability density for the average stellar mass $\langle M \rangle$ in the lensing galaxy in solar units. (c) Probability density for the scale radius (\hat{r}_s) of the quasar source in Einstein units in which $\hat{r}_s = r_s / \langle M/M_\odot \rangle^{1/2}$ where $\langle M \rangle$ is the average mass of a star in the lensing galaxy. The dotted line assumes a uniform prior on the mass of the microlenses $0.1 \leq \langle M/M_\odot \rangle \leq 1.0$. (d) Probability density for the physical source size r_s where the dotted line was tabulated assuming the mass prior.

same luminosity (Morgan et al., 2010). While we were expecting a larger accretion disk than that predicted by Shakura & Sunyaev (1973), the size we measured is anomalously large for its black hole mass, making us suspicious of the accuracy of the Motta et al. (2017) result.

To test this hypothesis, we also calculated the theoretical thin disk size based on observed luminosity in the I-band. Using the derivation from Morgan et al. (2010), we have a size of

$$R_I = 2.83 \times 10^{15} \frac{1}{\sqrt{\cos i}} \left(\frac{D_{OS}}{r_H} \right) \left(\frac{\lambda_{I,obs}}{\mu m} \right)^{3/2} 10^{-0.2(I-19)} h^{-1} \text{cm}, \quad (10)$$

where D_{OS}/r_H is the angular diameter distance to the quasar in units of the Hubble radius, $\lambda_{I,obs}$ is the observed I-band wavelength, and I is the magnification-corrected magnitude. For WFI 2033, we find a face-on rest wavelength corrected ($\lambda_{rest} = 2500 \text{ \AA}$) size $\log(r_{lum}/\text{cm}) = 15.0492$. In Figure 11 we show that the luminosity-based measurement is on the Accretion Disk Size- Black Hole Mass relation line when it should instead be on the dot-dashed line corresponding to the prediction from thin disk theory.

We conclude that the actual black hole mass is probably larger than what Motta et al. (2017) predicted for three reasons. First, when comparing our microlensing-based measurement to the calculated luminosity-based size, and consistent with previous results, the microlensing size is ≈ 0.7 dex larger than the calculated luminosity based size. Second, almost all of the luminosity-based sizes in Figure 11 are much smaller than those predicted by the Accretion Disk Size- Black Hole Mass relation but the WFI 2033 luminosity-based size falls directly on the fit line. Third, the mass of the black hole was poorly constrained by Motta et al. (2017) who used a less than robust C III] emission line measurement. A larger black hole mass for WFI 2033 would bring the system into better agreement with the Accretion Disk Size- Black Hole Mass relation.

6. Conclusions

In this investigation we reduced and combined the data we obtained from the EULER and SMARTS telescopes to create a 13 season light curve, we made 400 magnification patterns for each of the four images from 10 different models of the lens galaxy, and we generated 40 billion trial light curves to fit to our observed light curves assigning each light curve a χ^2 value based on the goodness of fit. We ultimately applied Bayesian statistical methods to acquire the probability distribution for the size of the quasar accretion disk. Moving forward, we plan to make a more precise measurement of WFI 2033's black hole mass using the C IV and Mg II emission lines (e.g. Assef et al., 2011) from the existing spectrum of Morgan et al. (2004).

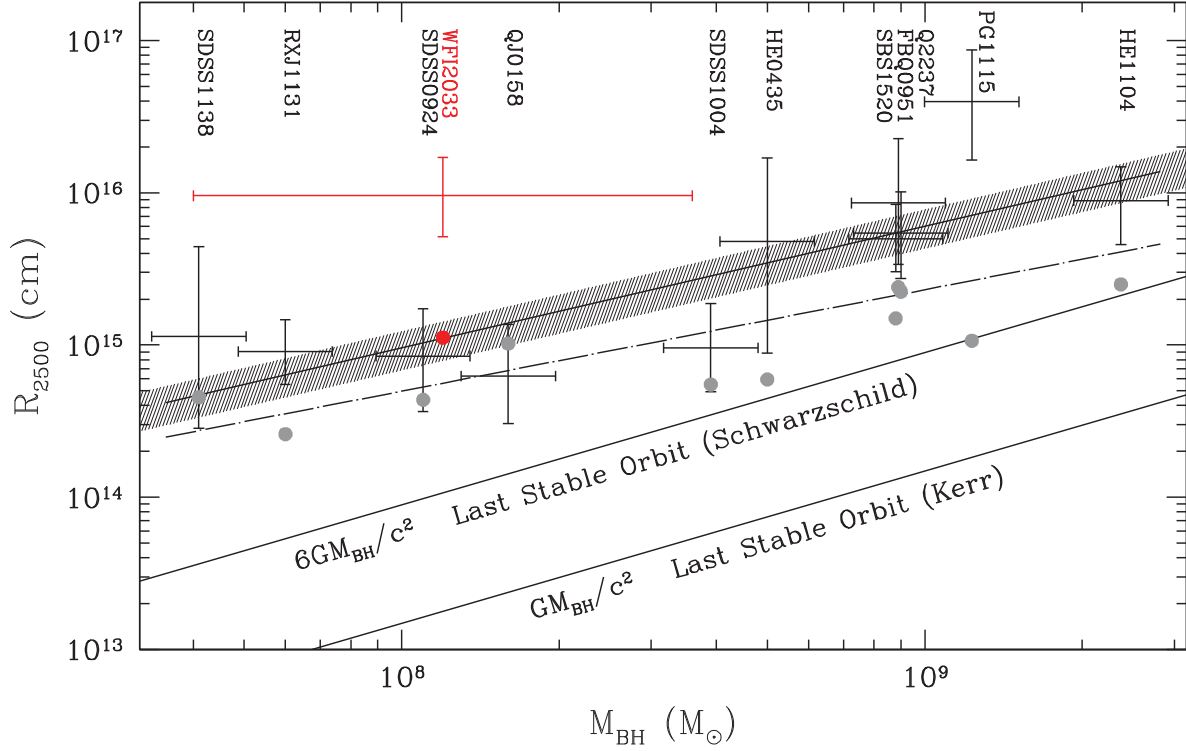


Fig. 11.—: Plot of inclination-corrected accretion disk size R_{2500} vs. black hole mass M_{BH} . The solid line through the data shows the best power-law fit to the data of Morgan et al. (2010) and the dot-dashed line shows the prediction from thin-disk theory assuming a luminosity equal to the Eddington luminosity and an efficiency of $\eta = .10$. The shaded band surrounding the best fit shows the expected variance due to inclination. The disk sizes were corrected to a rest wavelength of $\lambda_{rest} = 2500 \text{ \AA}$ and the black hole masses were estimated using emission line widths (Morgan et al., 2010). The points without error bars correspond to R_{2500} , magnification corrected, observed I-band fluxes. Note that the WFI 2033 values (shown in red) would be consistent with previous measurements for $M_{BH} \approx 5 \times 10^8 M_{\odot}$.

References

- Assef, R. J., Denney, K. D., Kochanek, C. S., et al. 2011, *ApJ*, 742, 93
- Bentz, M. C., Denney, K. D., Cackett, E. M., et al. 2006, *ApJ*, 651, 775
- Blaes, O. 2007, in *ASP Conf. Ser. 373, The Central Engine of Active Galactic Nuclei*, ed. L.C. Ho & J.-M. Wang (San Francisco: ASP), 75
- Chang, K. & Refsdal, S., 1979, *Nature*, 282, 561
- Cackett, E.M., Horne, K. & Winkler, H. 2007, *MNRAS*, 380, 669
- DePoy, D.L., Atwood, B., Belville, S.R., Brewer, D.F., Byard, P.L., Gould, A., Mason, J.A., O'Brien, T.P., Pappalardo, D.P., Pogge, R.W., Steinbrecher, D.P., & Tiega, E.J., 2003, *SPIE*, 4841, 827
- De Villiers, J.-P., Hawley, J.F. & Krolik, J.F. 2003, *ApJ*, 599, 1238
- Einstein, A. 1916, *Annalen der Physik*, 49, 769
- Elvis, M. et al. 1994, *ApJS*, 95, 1
- Hubeny, I. & Hubeny, V. 1997, *ApJ*, 484, L37
- Hubeny, I., Blaes, O., Krolik, J.H & Agol, E. 2001, *ApJ*, 559, 680
- Hinshaw, G., Weiland, J. L., Hill, R. S., et al. 2009, *ApJS*, 180, 225
- Kayser, R., Refsdal, S., & Stabell, R. 1986, *A&A*, 166, 36
- Keeton, C.R. 2001, preprint (astro-ph/0102340)
- Kochanek, C.S. 2004, *ApJ*, 605, 58
- Li, L.-X., Zimmerman, E.R., Narayan, R. & McClintock, J.E. 2005, *ApJS*, 157, 335
- Mediavilla, E. 2011, *Journal of Cosmology*, 17, 7331
- Morgan, N.D., & Caldwell, J.A.R., & Schechter, P.L., & Dressler, A., & Egami, E., & Rix, H.-W. 2004, *AJ*, 127, 2617
- Morgan, C. W., Kochanek, C. S., Morgan, N. D., & Falco, E. E. 2006, *ApJ*, 647, 874
- Morgan, C.W., Eyler, M.E., Kochanek, C.S., Morgan, N.D., Falco, E.E., Vuissoz, C., Courbin, F., & Meylan, G., *ApJ*, submitted
- Morgan, C.W., Kochanek, C.S., Morgan, N.D., & Falco, E.E. 2010, *ApJ*, 712, 1129

- Motta V., Mediavilla E., Rojas K., Falco E. E., Jimnez-Vicente J., Muoz J. A., 2017, ApJ, 835, 132
- Narayan, R., Barret, D. & McClintock, J.E. 1997, ApJ, 482, 448
- Navarro, J.F. Frenk, C.S. & White S.D.M. 1996, ApJ, 462, 563
- Page, D.N. & Thorne, K.S. 1974, ApJ, 191, 499
- Peterson, B. M. 1997, An Introduction to Active Galactic Nuclei (Cambridge UP: Cambridge)
- Reis, R.C., Reynolds, M.T., Miller, J.M., & Walton, D.J. 2014, Nature, 507, 207
- Sanders, D.B. et al., 1989, ApJ, 347, 29
- Schechter, P. L., & Wambsganss, J. 2002, ApJ, 580, 685
- Schmidt, M. 1963, Natur, 197, 1040
- Shakura, N.I. & Sunyaev, R.A. 1973, A&A, 24, 337
- Sluse, D., Chantry, V., Magain, P., Courbin, F., & Meylan, G. 2012, A&A, 538, A99
- Vuissoz, C., Courbin, F., Sluse, D., et al. 2008, A&A, 488, 481
- Wambsganss, J. 1998, Living Reviews in Relativity, 1, 12

A. Reduced Photometric Data

Table 2:: WFI2033–4723 Light Curves - SMARTS

HJD	Image A1	Image A2	Image B	Image C	χ^2/N_{dof}	Source
3082.897	2.747 ± 0.012	3.396 ± 0.021	3.425 ± 0.012	3.640 ± 0.015	1.6	SMARTS
3112.857	2.769 ± 0.017	3.411 ± 0.029	3.554 ± 0.014	3.638 ± 0.017	1.7	SMARTS
3138.866	2.835 ± 0.017	3.460 ± 0.030	3.610 ± 0.016	3.708 ± 0.019	3.0	SMARTS
3146.900	2.848 ± 0.015	3.448 ± 0.025	3.606 ± 0.013	3.718 ± 0.015	5.7	SMARTS
3154.840	2.870 ± 0.015	3.511 ± 0.025	3.635 ± 0.013	3.670 ± 0.015	2.9	SMARTS
3175.825	2.937 ± 0.011	3.502 ± 0.016	3.584 ± 0.011	3.751 ± 0.013	6.0	SMARTS
3184.777	2.948 ± 0.014	3.519 ± 0.023	3.601 ± 0.013	3.748 ± 0.016	1.8	SMARTS
3211.740	2.921 ± 0.014	3.572 ± 0.025	3.568 ± 0.013	3.737 ± 0.016	1.7	SMARTS
3282.634	2.996 ± 0.014	3.444 ± 0.020	3.544 ± 0.011	3.780 ± 0.014	3.0	SMARTS
3295.616	2.892 ± 0.013	3.566 ± 0.023	3.544 ± 0.012	3.794 ± 0.015	4.2	SMARTS
3298.566	2.931 ± 0.015	3.548 ± 0.025	3.564 ± 0.014	3.787 ± 0.017	1.4	SMARTS
3310.551	2.881 ± 0.013	3.578 ± 0.024	3.605 ± 0.013	3.789 ± 0.015	1.5	SMARTS
3320.551	3.081 ± 0.021	3.273 ± 0.024	3.602 ± 0.015	3.831 ± 0.019	4.0	SMARTS
3592.759	2.966 ± 0.016	3.607 ± 0.028	3.528 ± 0.014	3.890 ± 0.019	1.8	SMARTS
3625.668	2.881 ± 0.014	3.531 ± 0.024	3.463 ± 0.015	3.854 ± 0.022	1.5	SMARTS
3651.552	2.838 ± 0.017	3.475 ± 0.030	3.423 ± 0.013	3.824 ± 0.021	2.0	SMARTS
3661.571	2.893 ± 0.031	3.339 ± 0.045	3.445 ± 0.024	3.875 ± 0.038	1.0	SMARTS
3665.553	2.904 ± 0.017	3.363 ± 0.024	3.440 ± 0.013	3.801 ± 0.018	2.1	SMARTS
3675.522	2.895 ± 0.018	3.315 ± 0.025	3.411 ± 0.015	3.800 ± 0.020	2.2	SMARTS
3826.891	2.762 ± 0.018	3.483 ± 0.034	3.436 ± 0.016	3.681 ± 0.020	1.0	SMARTS
3832.855	2.742 ± 0.024	3.453 ± 0.045	3.553 ± 0.020	3.723 ± 0.026	4.0	SMARTS
3852.870	2.740 ± 0.015	3.495 ± 0.028	3.524 ± 0.015	3.697 ± 0.018	1.9	SMARTS
3863.788	2.736 ± 0.016	3.471 ± 0.030	3.570 ± 0.018	3.679 ± 0.020	4.7	SMARTS
3886.859	2.819 ± 0.012	3.486 ± 0.020	3.599 ± 0.014	3.666 ± 0.015	1.8	SMARTS
3937.732	2.942 ± 0.016	3.578 ± 0.028	3.517 ± 0.014	3.772 ± 0.018	1.6	SMARTS
3994.640	2.938 ± 0.019	3.281 ± 0.025	3.499 ± 0.014	3.785 ± 0.019	2.3	SMARTS
4021.575	2.932 ± 0.018	3.325 ± 0.027	3.598 ± 0.016	3.757 ± 0.020	1.5	SMARTS
4042.528	2.889 ± 0.027	3.478 ± 0.046	3.532 ± 0.025	3.738 ± 0.032	0.9	SMARTS
4050.555	2.921 ± 0.016	3.510 ± 0.026	3.494 ± 0.015	3.765 ± 0.018	4.4	SMARTS
4064.511	2.963 ± 0.041	3.462 ± 0.064	3.397 ± 0.036	3.728 ± 0.050	0.6	SMARTS
4207.876	2.773 ± 0.019	3.472 ± 0.036	3.540 ± 0.016	3.791 ± 0.022	3.5	SMARTS
4224.867	2.832 ± 0.023	3.400 ± 0.038	3.456 ± 0.020	3.763 ± 0.028	1.8	SMARTS
4234.918	2.811 ± 0.018	3.471 ± 0.031	3.374 ± 0.014	3.695 ± 0.020	0.9	SMARTS

Continued ...

Table 2:: WFI2033–4723 Light Curves - SMARTS

HJD	Image A1	Image A2	Image B	Image C	χ^2/N_{dof}	Source
4243.898	2.818 ± 0.015	3.450 ± 0.026	3.385 ± 0.013	3.713 ± 0.018	1.3	SMARTS
4293.829	2.703 ± 0.015	3.413 ± 0.028	3.399 ± 0.013	3.649 ± 0.017	1.3	SMARTS
4345.711	2.758 ± 0.021	3.381 ± 0.036	3.353 ± 0.016	3.700 ± 0.023	2.1	SMARTS
4363.622	2.796 ± 0.038	3.255 ± 0.057	3.304 ± 0.031	3.703 ± 0.048	0.3	SMARTS
4367.667	2.839 ± 0.030	3.259 ± 0.042	3.345 ± 0.024	3.675 ± 0.035	0.9	SMARTS
4371.624	2.768 ± 0.024	3.395 ± 0.043	3.357 ± 0.020	3.685 ± 0.029	0.8	SMARTS
4378.583	2.687 ± 0.014	3.449 ± 0.026	3.343 ± 0.012	3.680 ± 0.017	1.7	SMARTS
4387.542	2.690 ± 0.014	3.414 ± 0.026	3.343 ± 0.013	3.659 ± 0.017	1.6	SMARTS
4390.519	2.706 ± 0.012	3.407 ± 0.021	3.324 ± 0.012	3.648 ± 0.016	1.8	SMARTS
4394.534	2.696 ± 0.023	3.404 ± 0.043	3.311 ± 0.021	3.719 ± 0.031	0.9	SMARTS
4397.544	2.725 ± 0.020	3.276 ± 0.032	3.271 ± 0.017	3.697 ± 0.025	1.0	SMARTS
4407.520	2.693 ± 0.025	3.384 ± 0.046	3.257 ± 0.018	3.661 ± 0.028	1.0	SMARTS
4427.512	2.739 ± 0.037	3.233 ± 0.057	3.322 ± 0.032	3.680 ± 0.047	0.7	SMARTS
4550.907	2.589 ± 0.021	3.286 ± 0.039	3.349 ± 0.020	3.630 ± 0.028	3.8	SMARTS
4557.869	2.587 ± 0.013	3.304 ± 0.024	3.321 ± 0.012	3.623 ± 0.016	1.4	SMARTS
4564.904	2.519 ± 0.011	3.373 ± 0.021	3.339 ± 0.011	3.618 ± 0.014	3.0	SMARTS
4571.811	2.554 ± 0.015	3.369 ± 0.031	3.346 ± 0.013	3.569 ± 0.017	1.2	SMARTS
4588.916	2.637 ± 0.015	3.331 ± 0.027	3.373 ± 0.013	3.602 ± 0.017	2.5	SMARTS
4589.840	2.603 ± 0.014	3.354 ± 0.025	3.385 ± 0.012	3.570 ± 0.015	4.4	SMARTS
4596.807	2.637 ± 0.012	3.379 ± 0.022	3.393 ± 0.011	3.587 ± 0.014	1.7	SMARTS
4633.820	2.704 ± 0.021	3.350 ± 0.037	3.374 ± 0.017	3.703 ± 0.026	2.6	SMARTS
4653.812	2.706 ± 0.020	3.350 ± 0.036	3.379 ± 0.016	3.658 ± 0.023	0.9	SMARTS
4660.793	2.660 ± 0.015	3.403 ± 0.029	3.392 ± 0.013	3.677 ± 0.019	1.6	SMARTS
4678.731	2.744 ± 0.013	3.391 ± 0.022	3.376 ± 0.011	3.681 ± 0.015	4.4	SMARTS
4684.695	2.698 ± 0.012	3.482 ± 0.022	3.378 ± 0.011	3.630 ± 0.015	2.6	SMARTS
4716.731	2.667 ± 0.031	3.375 ± 0.058	3.363 ± 0.026	3.690 ± 0.038	0.6	SMARTS
4724.697	2.725 ± 0.020	3.348 ± 0.035	3.328 ± 0.019	3.676 ± 0.026	1.8	SMARTS
4732.649	2.729 ± 0.025	3.331 ± 0.042	3.324 ± 0.019	3.684 ± 0.027	1.2	SMARTS
4747.635	2.729 ± 0.017	3.432 ± 0.032	3.388 ± 0.014	3.691 ± 0.019	1.2	SMARTS
4754.586	2.765 ± 0.022	3.314 ± 0.036	3.379 ± 0.018	3.659 ± 0.024	0.5	SMARTS
4758.587	2.703 ± 0.012	3.408 ± 0.022	3.359 ± 0.011	3.671 ± 0.014	3.7	SMARTS
4783.521	2.705 ± 0.016	3.410 ± 0.029	3.349 ± 0.016	3.651 ± 0.021	1.0	SMARTS
4790.543	2.682 ± 0.012	3.456 ± 0.023	3.339 ± 0.011	3.690 ± 0.015	3.4	SMARTS
4797.550	2.686 ± 0.014	3.422 ± 0.026	3.366 ± 0.012	3.686 ± 0.015	2.2	SMARTS
5009.684	2.463 ± 0.014	3.193 ± 0.026	3.135 ± 0.011	3.551 ± 0.016	4.5	SMARTS

Continued ...

Table 2:: WFI2033–4723 Light Curves - SMARTS

HJD	Image A1	Image A2	Image B	Image C	χ^2/N_{dof}	Source
5021.762	2.461 ± 0.022	3.191 ± 0.043	2.993 ± 0.020	3.407 ± 0.031	1.1	SMARTS
5038.667	2.430 ± 0.014	3.130 ± 0.025	3.071 ± 0.010	3.549 ± 0.016	4.8	SMARTS
5043.671	2.421 ± 0.021	3.196 ± 0.042	3.023 ± 0.022	3.478 ± 0.035	0.5	SMARTS
5053.723	2.417 ± 0.016	3.153 ± 0.030	2.987 ± 0.012	3.480 ± 0.020	1.7	SMARTS
5072.652	2.393 ± 0.011	3.151 ± 0.021	3.020 ± 0.010	3.433 ± 0.015	1.8	SMARTS
5106.592	2.370 ± 0.019	3.074 ± 0.035	3.038 ± 0.015	3.415 ± 0.022	1.2	SMARTS
5127.553	2.372 ± 0.012	3.140 ± 0.022	3.092 ± 0.011	3.379 ± 0.014	2.6	SMARTS
5150.518	2.423 ± 0.017	3.090 ± 0.031	3.130 ± 0.013	3.421 ± 0.018	2.1	SMARTS
5326.806	2.420 ± 0.014	3.212 ± 0.028	3.232 ± 0.012	3.443 ± 0.016	1.3	SMARTS
5335.836	2.449 ± 0.013	3.183 ± 0.023	3.236 ± 0.012	3.483 ± 0.015	2.1	SMARTS
5353.802	2.473 ± 0.010	3.237 ± 0.019	3.271 ± 0.011	3.445 ± 0.012	2.9	SMARTS
5372.779	2.542 ± 0.017	3.229 ± 0.032	3.254 ± 0.017	3.514 ± 0.023	0.5	SMARTS
5379.848	2.533 ± 0.016	3.272 ± 0.030	3.280 ± 0.014	3.503 ± 0.018	1.0	SMARTS
5388.792	2.627 ± 0.017	3.193 ± 0.027	3.152 ± 0.011	3.601 ± 0.018	7.8	SMARTS
6407.908	2.534 ± 0.021	3.311 ± 0.041	3.103 ± 0.017	3.546 ± 0.026	2.8	SMARTS
6418.889	2.511 ± 0.012	3.257 ± 0.021	3.136 ± 0.011	3.635 ± 0.015	5.1	SMARTS
6431.908	2.498 ± 0.014	3.225 ± 0.027	3.123 ± 0.011	3.659 ± 0.018	8.7	SMARTS
6436.834	2.496 ± 0.017	3.298 ± 0.035	3.177 ± 0.016	3.627 ± 0.025	1.8	SMARTS
6458.851	2.546 ± 0.013	3.336 ± 0.025	3.180 ± 0.011	3.559 ± 0.015	4.1	SMARTS
6464.838	2.534 ± 0.017	3.373 ± 0.035	3.053 ± 0.014	3.578 ± 0.023	11.8	SMARTS
6488.762	2.620 ± 0.017	3.276 ± 0.030	3.230 ± 0.013	3.578 ± 0.018	2.4	SMARTS
6492.691	2.587 ± 0.017	3.282 ± 0.030	3.186 ± 0.014	3.598 ± 0.022	5.0	SMARTS
6508.687	2.589 ± 0.045	3.311 ± 0.088	3.142 ± 0.036	3.606 ± 0.060	0.9	SMARTS
6760.883	2.546 ± 0.016	3.251 ± 0.030	3.212 ± 0.014	3.589 ± 0.020	3.3	SMARTS
6825.834	2.594 ± 0.024	3.401 ± 0.049	3.289 ± 0.019	3.632 ± 0.029	1.2	SMARTS
6857.805	2.589 ± 0.017	3.367 ± 0.033	3.179 ± 0.012	3.665 ± 0.020	3.2	SMARTS
6944.600	2.546 ± 0.016	3.309 ± 0.031	3.131 ± 0.011	3.596 ± 0.017	4.9	SMARTS
7141.898	2.541 ± 0.014	3.320 ± 0.026	3.153 ± 0.012	3.622 ± 0.018	2.5	SMARTS
7150.873	2.607 ± 0.033	3.209 ± 0.057	3.149 ± 0.027	3.683 ± 0.048	2.1	SMARTS
7253.669	2.420 ± 0.013	3.237 ± 0.026	3.245 ± 0.012	3.503 ± 0.016	2.3	SMARTS
7255.638	2.406 ± 0.023	3.228 ± 0.047	3.274 ± 0.021	3.503 ± 0.030	0.7	SMARTS
7269.616	2.339 ± 0.014	3.304 ± 0.032	3.267 ± 0.013	3.577 ± 0.019	3.7	SMARTS
7278.583	2.458 ± 0.014	3.275 ± 0.028	3.266 ± 0.013	3.519 ± 0.018	2.0	SMARTS
7340.526	2.459 ± 0.012	3.374 ± 0.025	3.225 ± 0.012	3.556 ± 0.016	1.7	SMARTS
7344.525	2.509 ± 0.023	3.241 ± 0.044	3.222 ± 0.024	3.630 ± 0.036	0.9	SMARTS

Continued ...

Table 2:: WFI2033–4723 Light Curves - SMARTS

HJD	Image A1	Image A2	Image B	Image C	χ^2/N_{dof}	Source
7598.716	2.611 ± 0.021	3.338 ± 0.040	3.341 ± 0.020	3.605 ± 0.027	0.6	SMARTS
7603.680	2.619 ± 0.015	3.355 ± 0.027	3.364 ± 0.012	3.607 ± 0.017	1.5	SMARTS
7605.790	2.586 ± 0.015	3.347 ± 0.028	3.319 ± 0.013	3.633 ± 0.017	4.1	SMARTS
7608.765	2.620 ± 0.017	3.323 ± 0.031	3.289 ± 0.013	3.636 ± 0.019	1.1	SMARTS
7613.738	2.583 ± 0.018	3.406 ± 0.037	3.317 ± 0.016	3.614 ± 0.022	1.1	SMARTS
7652.639	2.665 ± 0.020	3.274 ± 0.033	3.211 ± 0.015	3.462 ± 0.020	7.7	SMARTS
7661.601	2.634 ± 0.019	3.272 ± 0.032	3.320 ± 0.014	3.547 ± 0.020	2.3	SMARTS
7695.556	2.662 ± 0.017	3.344 ± 0.031	3.231 ± 0.013	3.587 ± 0.020	3.1	SMARTS
7702.583	2.610 ± 0.019	3.373 ± 0.038	3.302 ± 0.018	3.547 ± 0.023	2.4	SMARTS
7856.868	2.866 ± 0.032	3.130 ± 0.038	3.531 ± 0.026	3.762 ± 0.035	1.0	SMARTS
7867.882	2.676 ± 0.015	3.471 ± 0.029	3.536 ± 0.015	3.691 ± 0.018	2.5	SMARTS
7872.884	2.687 ± 0.014	3.478 ± 0.027	3.452 ± 0.014	3.736 ± 0.019	2.1	SMARTS
7877.840	2.700 ± 0.017	3.516 ± 0.034	3.497 ± 0.017	3.701 ± 0.022	1.6	SMARTS
7894.808	2.717 ± 0.020	3.462 ± 0.038	3.511 ± 0.018	3.723 ± 0.023	3.4	SMARTS
7904.766	2.697 ± 0.016	3.493 ± 0.031	3.520 ± 0.016	3.714 ± 0.020	4.4	SMARTS
7914.785	2.725 ± 0.024	3.372 ± 0.041	3.499 ± 0.027	3.756 ± 0.035	0.7	SMARTS

HJD is the Heliocentric Julian Day -2450000 days. The goodness of fit of the image, χ^2/N_{dof} , is used to rescale the formal uncertainties by a factor of $(\chi^2/N_{dof})^{1/2}$. The Image A1-C columns give the magnitudes of the quasar images relative to the comparison stars.

Table 3:: WFI2033–4723 Light Curves - EULER

HJD	Image A1	Image A2	Image B	Image C	χ^2/N_{dof}	Source
5485.659	2.628 ± 0.008	3.285 ± 0.013	3.348 ± 0.007	3.597 ± 0.009	2.4	EULER
5488.637	2.644 ± 0.008	3.281 ± 0.013	3.341 ± 0.007	3.579 ± 0.008	3.8	EULER
5503.592	2.654 ± 0.006	3.294 ± 0.009	3.368 ± 0.005	3.615 ± 0.006	10.5	EULER
5506.571	2.662 ± 0.007	3.293 ± 0.010	3.378 ± 0.006	3.629 ± 0.007	6.3	EULER
5655.905	2.764 ± 0.002	3.518 ± 0.004	3.505 ± 0.003	3.684 ± 0.004	2.8	EULER
5656.910	2.742 ± 0.007	3.564 ± 0.013	3.499 ± 0.007	3.697 ± 0.008	6.1	EULER
5667.908	2.768 ± 0.001	3.506 ± 0.002	3.589 ± 0.002	3.732 ± 0.002	6.6	EULER
5674.897	2.792 ± 0.008	3.534 ± 0.014	3.569 ± 0.008	3.729 ± 0.009	2.2	EULER
5678.879	2.772 ± 0.007	3.528 ± 0.012	3.575 ± 0.006	3.733 ± 0.007	7.8	EULER
5682.896	2.773 ± 0.007	3.541 ± 0.012	3.587 ± 0.007	3.731 ± 0.008	5.7	EULER
5686.849	2.791 ± 0.007	3.518 ± 0.012	3.583 ± 0.007	3.742 ± 0.008	3.4	EULER
5694.851	2.760 ± 0.007	3.587 ± 0.012	3.602 ± 0.007	3.744 ± 0.008	11.0	EULER
5712.864	2.832 ± 0.006	3.536 ± 0.009	3.524 ± 0.006	3.829 ± 0.007	8.7	EULER
5723.776	2.860 ± 0.008	3.565 ± 0.013	3.495 ± 0.007	3.786 ± 0.009	2.6	EULER
5725.771	2.828 ± 0.002	3.616 ± 0.005	3.500 ± 0.004	3.784 ± 0.005	3.7	EULER
5739.722	2.861 ± 0.009	3.554 ± 0.016	3.431 ± 0.007	3.799 ± 0.009	2.5	EULER
5762.714	2.758 ± 0.008	3.549 ± 0.016	3.437 ± 0.008	3.792 ± 0.011	3.1	EULER
5766.821	2.746 ± 0.009	3.510 ± 0.016	3.387 ± 0.006	3.865 ± 0.010	3.4	EULER
5770.741	2.723 ± 0.007	3.534 ± 0.013	3.430 ± 0.006	3.807 ± 0.009	3.7	EULER
5775.621	2.785 ± 0.016	3.381 ± 0.028	3.449 ± 0.013	3.791 ± 0.018	1.1	EULER
5779.607	2.710 ± 0.007	3.515 ± 0.013	3.431 ± 0.006	3.783 ± 0.008	3.4	EULER
5783.712	2.725 ± 0.007	3.448 ± 0.013	3.414 ± 0.008	3.824 ± 0.011	2.8	EULER
5794.685	2.704 ± 0.006	3.473 ± 0.011	3.430 ± 0.006	3.805 ± 0.008	4.5	EULER
5804.569	2.712 ± 0.008	3.503 ± 0.015	3.501 ± 0.007	3.716 ± 0.009	2.9	EULER
5807.536	2.711 ± 0.001	3.500 ± 0.002	3.501 ± 0.002	3.720 ± 0.002	4.5	EULER
5815.552	2.702 ± 0.008	3.500 ± 0.015	3.528 ± 0.009	3.808 ± 0.011	4.9	EULER
5818.636	2.732 ± 0.007	3.454 ± 0.011	3.493 ± 0.007	3.803 ± 0.009	5.3	EULER
5820.656	2.741 ± 0.007	3.452 ± 0.011	3.500 ± 0.007	3.803 ± 0.009	5.0	EULER
5824.700	2.755 ± 0.009	3.432 ± 0.015	3.507 ± 0.007	3.798 ± 0.009	4.5	EULER
5827.557	2.715 ± 0.008	3.438 ± 0.013	3.575 ± 0.007	3.835 ± 0.010	8.9	EULER
5831.537	2.748 ± 0.005	3.464 ± 0.008	3.545 ± 0.006	3.773 ± 0.007	16.3	EULER
5839.610	2.783 ± 0.011	3.467 ± 0.020	3.545 ± 0.009	3.851 ± 0.013	3.4	EULER
5842.521	2.775 ± 0.009	3.536 ± 0.016	3.583 ± 0.009	3.805 ± 0.012	2.7	EULER
5854.529	2.813 ± 0.008	3.544 ± 0.014	3.585 ± 0.007	3.794 ± 0.009	4.1	EULER

Continued ...

Table 3:: WFI2033–4723 Light Curves - EULER

HJD	Image A1	Image A2	Image B	Image C	χ^2/N_{dof}	Source
5857.517	2.830 ± 0.007	3.580 ± 0.013	3.576 ± 0.006	3.763 ± 0.008	3.2	EULER
5865.500	2.849 ± 0.018	3.579 ± 0.034	3.608 ± 0.019	3.799 ± 0.024	0.9	EULER
5865.512	2.852 ± 0.009	3.534 ± 0.015	3.577 ± 0.008	3.785 ± 0.010	2.8	EULER
5869.535	2.819 ± 0.009	3.617 ± 0.017	3.583 ± 0.008	3.777 ± 0.010	2.5	EULER
5873.574	2.884 ± 0.017	3.509 ± 0.030	3.563 ± 0.013	3.847 ± 0.019	1.3	EULER
5887.557	2.916 ± 0.007	3.587 ± 0.013	3.542 ± 0.007	3.816 ± 0.008	3.2	EULER
5896.532	2.907 ± 0.010	3.653 ± 0.019	3.548 ± 0.009	3.810 ± 0.011	1.5	EULER
5897.530	2.912 ± 0.011	3.600 ± 0.020	3.525 ± 0.009	3.841 ± 0.012	2.4	EULER
6011.897	2.783 ± 0.001	3.567 ± 0.001	3.540 ± 0.001	3.775 ± 0.001	5.0	EULER
6015.909	2.759 ± 0.009	3.585 ± 0.019	3.602 ± 0.009	3.758 ± 0.011	7.1	EULER
6017.894	2.778 ± 0.007	3.558 ± 0.013	3.561 ± 0.007	3.757 ± 0.008	8.2	EULER
6018.905	2.808 ± 0.008	3.554 ± 0.015	3.550 ± 0.007	3.763 ± 0.009	2.3	EULER
6023.906	2.796 ± 0.009	3.601 ± 0.018	3.597 ± 0.009	3.780 ± 0.011	4.9	EULER
6028.900	2.822 ± 0.007	3.581 ± 0.012	3.589 ± 0.007	3.826 ± 0.009	4.8	EULER
6029.911	2.828 ± 0.009	3.587 ± 0.016	3.585 ± 0.008	3.812 ± 0.010	2.4	EULER
6047.869	2.811 ± 0.008	3.596 ± 0.015	3.588 ± 0.007	3.829 ± 0.009	7.3	EULER
6050.863	2.821 ± 0.008	3.559 ± 0.014	3.581 ± 0.007	3.865 ± 0.009	6.6	EULER
6058.888	2.810 ± 0.008	3.617 ± 0.014	3.565 ± 0.007	3.914 ± 0.011	4.9	EULER
6070.935	2.891 ± 0.007	3.480 ± 0.010	3.496 ± 0.007	3.897 ± 0.009	9.5	EULER
6092.942	2.864 ± 0.011	3.522 ± 0.019	3.516 ± 0.008	3.878 ± 0.012	3.6	EULER
6102.712	2.797 ± 0.007	3.577 ± 0.012	3.622 ± 0.007	3.891 ± 0.008	8.5	EULER
6109.823	2.854 ± 0.008	3.515 ± 0.013	3.575 ± 0.008	3.929 ± 0.010	7.4	EULER
6125.707	2.830 ± 0.008	3.577 ± 0.015	3.649 ± 0.007	3.902 ± 0.010	6.0	EULER
6129.706	2.857 ± 0.008	3.579 ± 0.015	3.632 ± 0.009	3.894 ± 0.012	5.8	EULER
6138.590	2.882 ± 0.011	3.600 ± 0.020	3.673 ± 0.010	3.865 ± 0.013	3.3	EULER
6151.591	2.899 ± 0.009	3.581 ± 0.017	3.630 ± 0.008	3.893 ± 0.010	2.7	EULER
6185.503	2.854 ± 0.012	3.592 ± 0.021	3.569 ± 0.012	3.942 ± 0.016	3.0	EULER
6185.515	2.855 ± 0.007	3.616 ± 0.011	3.567 ± 0.007	3.930 ± 0.009	7.4	EULER
6190.528	2.867 ± 0.007	3.591 ± 0.013	3.548 ± 0.007	3.940 ± 0.009	6.8	EULER
6194.537	2.864 ± 0.013	3.623 ± 0.025	3.533 ± 0.011	3.919 ± 0.018	1.3	EULER
6195.693	2.901 ± 0.007	3.562 ± 0.013	3.466 ± 0.007	3.914 ± 0.011	3.7	EULER
6217.615	2.860 ± 0.008	3.545 ± 0.014	3.405 ± 0.006	3.925 ± 0.009	6.2	EULER
6221.532	2.845 ± 0.009	3.566 ± 0.015	3.441 ± 0.007	3.931 ± 0.010	3.0	EULER
6224.554	2.819 ± 0.011	3.594 ± 0.022	3.439 ± 0.010	3.915 ± 0.015	1.4	EULER
6225.544	2.821 ± 0.002	3.583 ± 0.005	3.473 ± 0.004	3.895 ± 0.006	1.4	EULER

Continued ...

Table 3:: WFI2033–4723 Light Curves - EULER

HJD	Image A1	Image A2	Image B	Image C	χ^2/N_{dof}	Source
6232.501	2.831 ± 0.002	3.635 ± 0.005	3.400 ± 0.004	3.825 ± 0.005	0.8	EULER
6232.513	2.794 ± 0.010	3.588 ± 0.020	3.456 ± 0.008	3.869 ± 0.012	1.3	EULER
6236.552	2.816 ± 0.007	3.513 ± 0.012	3.392 ± 0.006	3.891 ± 0.008	5.7	EULER
6248.524	2.814 ± 0.008	3.511 ± 0.013	3.339 ± 0.006	3.837 ± 0.009	6.1	EULER
6251.522	2.773 ± 0.007	3.548 ± 0.013	3.348 ± 0.006	3.824 ± 0.009	5.2	EULER
6255.521	2.795 ± 0.005	3.552 ± 0.009	3.351 ± 0.006	3.811 ± 0.010	1.5	EULER
6387.892	2.479 ± 0.006	3.290 ± 0.011	3.221 ± 0.006	3.618 ± 0.007	7.7	EULER
6391.909	2.507 ± 0.007	3.293 ± 0.014	3.223 ± 0.007	3.622 ± 0.009	2.9	EULER
6396.909	2.470 ± 0.006	3.336 ± 0.012	3.229 ± 0.006	3.597 ± 0.008	6.5	EULER
6401.916	2.483 ± 0.007	3.317 ± 0.013	3.244 ± 0.007	3.619 ± 0.009	6.7	EULER
6405.897	2.481 ± 0.008	3.338 ± 0.016	3.201 ± 0.008	3.597 ± 0.011	1.5	EULER
6426.900	2.491 ± 0.010	3.308 ± 0.018	3.261 ± 0.009	3.582 ± 0.014	1.8	EULER
6435.872	2.502 ± 0.006	3.288 ± 0.010	3.276 ± 0.006	3.643 ± 0.008	6.9	EULER
6443.779	2.504 ± 0.013	3.299 ± 0.027	3.295 ± 0.013	3.580 ± 0.018	1.3	EULER
6447.755	2.507 ± 0.006	3.321 ± 0.012	3.284 ± 0.006	3.574 ± 0.007	4.3	EULER
6451.826	2.546 ± 0.006	3.282 ± 0.011	3.284 ± 0.006	3.618 ± 0.008	3.0	EULER
6455.899	2.563 ± 0.001	3.311 ± 0.003	3.253 ± 0.002	3.624 ± 0.003	1.9	EULER
6460.692	2.555 ± 0.009	3.353 ± 0.017	3.296 ± 0.008	3.595 ± 0.010	2.9	EULER
6468.728	2.553 ± 0.008	3.347 ± 0.016	3.317 ± 0.008	3.600 ± 0.010	2.6	EULER
6472.831	2.558 ± 0.007	3.313 ± 0.011	3.252 ± 0.006	3.645 ± 0.008	4.6	EULER
6476.840	2.565 ± 0.007	3.305 ± 0.013	3.274 ± 0.006	3.644 ± 0.008	3.7	EULER
6487.905	2.579 ± 0.006	3.289 ± 0.010	3.242 ± 0.005	3.571 ± 0.006	5.5	EULER
6491.597	2.555 ± 0.008	3.320 ± 0.016	3.288 ± 0.007	3.603 ± 0.009	2.3	EULER
6507.754	2.583 ± 0.006	3.325 ± 0.009	3.252 ± 0.005	3.629 ± 0.006	4.7	EULER
6515.817	2.596 ± 0.007	3.313 ± 0.012	3.277 ± 0.005	3.622 ± 0.007	3.1	EULER
6519.698	2.570 ± 0.005	3.276 ± 0.009	3.272 ± 0.005	3.705 ± 0.007	15.2	EULER
6523.581	2.565 ± 0.008	3.387 ± 0.015	3.310 ± 0.007	3.607 ± 0.009	3.7	EULER
6536.594	2.559 ± 0.008	3.355 ± 0.015	3.290 ± 0.007	3.651 ± 0.010	2.6	EULER
6541.644	2.579 ± 0.008	3.313 ± 0.013	3.240 ± 0.007	3.681 ± 0.010	4.5	EULER
6544.573	2.564 ± 0.008	3.345 ± 0.015	3.283 ± 0.007	3.674 ± 0.011	2.3	EULER
6548.724	2.604 ± 0.008	3.283 ± 0.013	3.203 ± 0.006	3.672 ± 0.008	6.0	EULER
6565.497	2.567 ± 0.009	3.349 ± 0.016	3.253 ± 0.007	3.597 ± 0.010	1.8	EULER
6565.509	2.546 ± 0.009	3.348 ± 0.018	3.237 ± 0.008	3.607 ± 0.011	1.6	EULER
6569.521	2.530 ± 0.005	3.353 ± 0.009	3.226 ± 0.005	3.647 ± 0.007	5.0	EULER
6572.558	2.548 ± 0.005	3.301 ± 0.008	3.203 ± 0.005	3.659 ± 0.006	8.6	EULER

Continued ...

Table 3:: WFI2033–4723 Light Curves - EULER

HJD	Image A1	Image A2	Image B	Image C	χ^2/N_{dof}	Source
6576.549	2.523 ± 0.006	3.315 ± 0.010	3.221 ± 0.005	3.666 ± 0.007	6.3	EULER
6581.604	2.541 ± 0.007	3.249 ± 0.013	3.203 ± 0.006	3.669 ± 0.009	6.1	EULER
6584.628	2.535 ± 0.008	3.281 ± 0.014	3.225 ± 0.007	3.615 ± 0.010	3.2	EULER
6599.552	2.515 ± 0.006	3.293 ± 0.010	3.209 ± 0.005	3.596 ± 0.006	5.5	EULER
6600.574	2.518 ± 0.005	3.249 ± 0.008	3.198 ± 0.005	3.596 ± 0.006	11.9	EULER
6604.538	2.527 ± 0.007	3.236 ± 0.013	3.191 ± 0.006	3.631 ± 0.008	3.9	EULER
6609.540	2.511 ± 0.005	3.262 ± 0.009	3.197 ± 0.005	3.590 ± 0.007	8.2	EULER
6612.521	2.519 ± 0.008	3.276 ± 0.015	3.190 ± 0.007	3.608 ± 0.009	3.1	EULER
6616.521	2.524 ± 0.009	3.328 ± 0.017	3.216 ± 0.007	3.560 ± 0.010	1.8	EULER
6745.906	2.533 ± 0.002	3.291 ± 0.003	3.310 ± 0.003	3.609 ± 0.004	2.9	EULER
6765.911	2.523 ± 0.006	3.388 ± 0.012	3.368 ± 0.007	3.555 ± 0.008	8.7	EULER
6775.899	2.492 ± 0.006	3.377 ± 0.010	3.371 ± 0.006	3.595 ± 0.007	7.1	EULER
6781.853	2.540 ± 0.007	3.307 ± 0.013	3.378 ± 0.006	3.602 ± 0.008	3.5	EULER
6789.900	2.543 ± 0.007	3.303 ± 0.013	3.363 ± 0.007	3.624 ± 0.009	2.4	EULER
6793.875	2.549 ± 0.007	3.327 ± 0.013	3.390 ± 0.008	3.636 ± 0.010	4.4	EULER
6797.924	2.551 ± 0.009	3.315 ± 0.018	3.309 ± 0.010	3.696 ± 0.014	2.4	EULER
6803.883	2.581 ± 0.007	3.346 ± 0.012	3.334 ± 0.006	3.659 ± 0.009	4.2	EULER
6805.832	2.574 ± 0.006	3.370 ± 0.011	3.364 ± 0.006	3.614 ± 0.007	5.3	EULER
6814.894	2.631 ± 0.006	3.331 ± 0.010	3.288 ± 0.005	3.655 ± 0.007	6.9	EULER
6818.896	2.631 ± 0.009	3.319 ± 0.015	3.278 ± 0.009	3.657 ± 0.012	2.6	EULER
6822.706	2.647 ± 0.013	3.363 ± 0.024	3.353 ± 0.011	3.604 ± 0.015	1.3	EULER
6834.749	2.596 ± 0.006	3.370 ± 0.010	3.370 ± 0.005	3.648 ± 0.007	6.8	EULER
6846.826	2.596 ± 0.006	3.331 ± 0.010	3.268 ± 0.005	3.677 ± 0.007	8.1	EULER
6874.560	2.578 ± 0.009	3.390 ± 0.017	3.279 ± 0.007	3.623 ± 0.010	1.7	EULER
6888.633	2.540 ± 0.006	3.350 ± 0.011	3.261 ± 0.006	3.671 ± 0.008	5.0	EULER
6908.528	2.539 ± 0.009	3.320 ± 0.018	3.292 ± 0.009	3.598 ± 0.012	1.8	EULER
6930.589	2.531 ± 0.006	3.301 ± 0.010	3.204 ± 0.005	3.646 ± 0.007	5.2	EULER
6937.568	2.531 ± 0.008	3.286 ± 0.015	3.194 ± 0.007	3.654 ± 0.011	3.1	EULER
6943.603	2.547 ± 0.005	3.267 ± 0.009	3.187 ± 0.005	3.614 ± 0.006	8.0	EULER
6947.525	2.525 ± 0.008	3.300 ± 0.014	3.203 ± 0.007	3.647 ± 0.010	3.1	EULER
6950.609	2.558 ± 0.008	3.274 ± 0.013	3.200 ± 0.006	3.601 ± 0.008	3.5	EULER
6954.612	2.542 ± 0.005	3.287 ± 0.009	3.208 ± 0.005	3.577 ± 0.006	11.6	EULER
6963.579	2.515 ± 0.008	3.284 ± 0.016	3.192 ± 0.007	3.610 ± 0.010	2.7	EULER
6974.526	2.505 ± 0.007	3.292 ± 0.014	3.224 ± 0.006	3.574 ± 0.008	3.1	EULER
6990.516	2.547 ± 0.013	3.272 ± 0.024	3.226 ± 0.011	3.549 ± 0.015	1.4	EULER

Continued ...

Table 3:: WFI2033–4723 Light Curves - EULER

HJD	Image A1	Image A2	Image B	Image C	χ^2/N_{dof}	Source
7113.905	2.549 ± 0.008	3.370 ± 0.016	3.300 ± 0.007	3.628 ± 0.009	2.3	EULER
7117.910	2.562 ± 0.011	3.362 ± 0.022	3.334 ± 0.010	3.587 ± 0.012	2.2	EULER
7123.909	2.568 ± 0.008	3.355 ± 0.016	3.313 ± 0.007	3.645 ± 0.010	2.4	EULER
7126.883	2.541 ± 0.006	3.376 ± 0.011	3.297 ± 0.006	3.639 ± 0.007	5.9	EULER
7138.858	2.544 ± 0.007	3.370 ± 0.013	3.273 ± 0.006	3.577 ± 0.008	3.2	EULER
7141.852	2.531 ± 0.007	3.364 ± 0.014	3.269 ± 0.006	3.588 ± 0.008	4.6	EULER
7145.844	2.560 ± 0.010	3.324 ± 0.019	3.238 ± 0.008	3.614 ± 0.011	1.6	EULER
7153.793	2.521 ± 0.008	3.354 ± 0.015	3.225 ± 0.007	3.603 ± 0.009	4.1	EULER
7157.888	2.535 ± 0.005	3.316 ± 0.008	3.193 ± 0.005	3.642 ± 0.007	7.8	EULER
7161.828	2.507 ± 0.007	3.391 ± 0.014	3.224 ± 0.007	3.595 ± 0.009	3.6	EULER
7170.829	2.490 ± 0.005	3.353 ± 0.009	3.209 ± 0.004	3.628 ± 0.006	4.3	EULER
7178.703	2.505 ± 0.014	3.247 ± 0.028	3.172 ± 0.011	3.578 ± 0.017	1.2	EULER
7186.875	2.450 ± 0.006	3.272 ± 0.011	3.132 ± 0.005	3.625 ± 0.008	4.2	EULER
7189.909	2.460 ± 0.007	3.233 ± 0.013	3.108 ± 0.006	3.620 ± 0.008	3.8	EULER
7193.878	2.428 ± 0.006	3.252 ± 0.010	3.091 ± 0.005	3.640 ± 0.007	10.5	EULER
7196.876	2.442 ± 0.007	3.226 ± 0.013	3.090 ± 0.006	3.652 ± 0.009	5.5	EULER
7200.681	2.441 ± 0.007	3.289 ± 0.013	3.130 ± 0.006	3.546 ± 0.008	3.3	EULER
7220.648	2.414 ± 0.007	3.248 ± 0.013	3.204 ± 0.006	3.547 ± 0.007	4.4	EULER
7227.605	2.390 ± 0.007	3.257 ± 0.014	3.205 ± 0.006	3.519 ± 0.008	2.7	EULER
7258.518	2.424 ± 0.007	3.286 ± 0.013	3.236 ± 0.006	3.457 ± 0.007	4.0	EULER
7263.564	2.412 ± 0.008	3.299 ± 0.016	3.274 ± 0.009	3.499 ± 0.011	2.7	EULER
7267.530	2.429 ± 0.005	3.296 ± 0.009	3.272 ± 0.005	3.492 ± 0.006	6.5	EULER
7270.537	2.440 ± 0.007	3.271 ± 0.014	3.291 ± 0.006	3.504 ± 0.008	2.5	EULER
7278.519	2.447 ± 0.006	3.315 ± 0.011	3.294 ± 0.006	3.501 ± 0.007	4.8	EULER
7293.582	2.441 ± 0.006	3.308 ± 0.010	3.242 ± 0.006	3.612 ± 0.007	9.5	EULER
7491.891	2.518 ± 0.007	3.307 ± 0.012	3.306 ± 0.006	3.615 ± 0.007	2.4	EULER
7507.870	2.508 ± 0.007	3.345 ± 0.014	3.328 ± 0.007	3.582 ± 0.008	2.2	EULER
7536.937	2.542 ± 0.020	3.304 ± 0.040	3.361 ± 0.020	3.643 ± 0.028	0.8	EULER
7557.851	2.575 ± 0.006	3.383 ± 0.011	3.335 ± 0.006	3.629 ± 0.008	4.1	EULER
7575.652	2.577 ± 0.006	3.353 ± 0.011	3.361 ± 0.005	3.575 ± 0.006	6.3	EULER
7590.677	2.570 ± 0.006	3.373 ± 0.011	3.371 ± 0.007	3.596 ± 0.009	5.4	EULER
7596.577	2.603 ± 0.010	3.332 ± 0.018	3.363 ± 0.008	3.593 ± 0.010	2.0	EULER
7599.776	2.579 ± 0.007	3.349 ± 0.013	3.315 ± 0.006	3.618 ± 0.008	4.5	EULER
7609.557	2.600 ± 0.007	3.350 ± 0.013	3.340 ± 0.006	3.607 ± 0.007	3.9	EULER
7647.656	2.590 ± 0.008	3.294 ± 0.015	3.322 ± 0.008	3.636 ± 0.010	3.0	EULER

Continued ...

Table 3:: WFI2033–4723 Light Curves - EULER

HJD	Image A1	Image A2	Image B	Image C	χ^2/N_{dof}	Source
7651.684	2.587 ± 0.006	3.314 ± 0.011	3.336 ± 0.006	3.618 ± 0.007	7.2	EULER
7671.581	2.581 ± 0.002	3.380 ± 0.004	3.373 ± 0.003	3.638 ± 0.004	3.3	EULER
7691.574	2.630 ± 0.007	3.336 ± 0.012	3.329 ± 0.006	3.640 ± 0.007	5.1	EULER
7696.536	2.618 ± 0.005	3.354 ± 0.008	3.337 ± 0.005	3.589 ± 0.006	21.9	EULER

HJD is the Heliocentric Julian Day -2450000 days. The goodness of fit of the image, χ^2/N_{dof} , is used to rescale the formal uncertainties by a factor of $(\chi^2/N_{dof})^{1/2}$. The Image A1-C columns give the magnitudes of the quasar images relative to the comparison stars. The relatively larger χ^2/N_{dof} values in the EULER light curves compared to the SMARTS light curves result from the smaller pixels in the EULER detector. The quasar images are formally oversampled by the EULER detector, so on marginal nights many more pixels contribute to the the noise in the residuals following subtraction of the PSF fit.

B. Glossary of Terms

angular diameter distance – a measure of distance to an object defined by the ratio of an object’s projected physical diameter to the angle it subtends on the sky. Because the universe is expanding, the angular diameter distance term contains a factor of H_0 .

cosmic microwave background (CMB) radiation – blackbody radiation peaking at about 3 kelvin that fills the universe and is thought to be the afterglow of the Big Bang. Because the radiation is isotropic, the peculiar motion of the Sun (i.e., the motion that is not due to the Hubble flow) causes an observable dipolar Doppler shift in the background that permits a measurement of the observer’s velocity.

de Vaucouleurs profile – a commonly used empirical fit to the surface brightness observed in elliptical galaxies. It is also known as the $r^{1/4}$ law due to the $r^{1/4}$ dependence in the exponent.

Eddington luminosity – the maximum radiated power at which the quasar can remain in equilibrium.

h – a dimensionless number parameterizing the rate of expansion of the universe. In cosmology, the Hubble constant $H_0 = 100h \text{ km s}^{-1} \text{ Mpc}^{-1}$. This constant sets the proportionality between the distance to celestial objects and their recessional velocity along the line of sight due to the expansion of the universe. This recession is often termed the “Hubble flow.”

Heliocentric Julian Day (HJD) – the continuous number of days since the beginning of the Julian Period (starting at noon on Monday, January 1, 4713 BC in the proleptic Julian calendar) corrected for differences in the Earth’s position with respect to the Sun.

magnitude – a logarithmic measure of an object’s intrinsic brightness across a given wavelength range. Brighter objects have lower magnitudes, and a difference of five magnitudes corresponds to a factor of 100 in brightness ($\Delta m = -2.5 \log(\frac{f_1}{f_2})$).

Navarro-Frenk-White (NFW) profile – a commonly used model of the spatial distribution of dark matter in a galaxy’s dark matter halo in the standard Cold Dark Matter cosmogony.

redshift (z) – a cosmological quantity that characterizes the distance to an object; specifically, the “cosmological redshift” is the amount by which an object’s rest-frame radiation is shifted to longer wavelengths due to the expansion of space. Since more distant objects are subject to faster recession in the Hubble flow (see the above discussion of h), their emitted light is more redshifted. Redshift is given by

$$1 + z = \frac{R_{now}}{R_{then}} = \frac{\lambda_{observed}}{\lambda_{emitted}}. \quad (\text{B1})$$

Here, $\frac{R_{now}}{R_{then}}$ is the ratio of the current scale of the universe to its scale when light was

emitted from a distant object, and $\frac{\lambda_{\text{observed}}}{\lambda_{\text{emitted}}}$ is the ratio of the light's wavelength as measured by the observer and its wavelength when it was emitted from the distant object.

rest-frame effective wavelength – the wavelength at the centroid of the observing band, adjusted for cosmological redshift.

seeing – a term that refers to the blurring of images due to the distortions caused by perturbations in the Earth's atmosphere. Seeing can be quantified at any given moment as the angular full width at half maximum of a point source in an exposure taken under existing atmospheric conditions.